A&A 664, A16 (2022)
https://doi.org/10.1051/0004-6361/202141382

Astronomy & Astrophysics

The BINGO Project

III. Optical design and optimization of the focal plane

Filipe B. Abdalla[1,2,3,4], Alessandro Marins[2], Pablo Motta[2], Elcio Abdalla[2], Rafael M. Ribeiro[2], Carlos A. Wuensche[3], Jacques Delabrouille[5,6,7], Karin S. F. Fornazier[2,3], Vincenzo Liccardo[3], Bruno Maffei[8], Eduardo J. de Mericia[3], Carlos H. N. Otobone[2], Juliana F. R. dos Santos[2], Gustavo B. Silva[2], Jordany Vieira[2], João A. M. Barretos[2], Luciano Barosi[9], Francisco A. Brito[9], Amilcar R. Queiroz[9], Thyrso Villela[3,10,11], Bin Wang[12,13], Andre A. Costa[12], Elisa G. M. Ferreira[2,14], Ricardo G. Landim[15], Camila Paiva Novaes[3], Michael W. Peel[16,17], Larissa Santos[12,13], Marcelo V. dos Santos[9], and Jiajun Zhang[18]

(Affiliations can be found after the references)

Received 25 May 2021 / Accepted 2 March 2022

ABSTRACT

Context. The Baryon Acoustic Oscillations from Integrated Neutral Gas Observations (BINGO) telescope was designed to measure the fluctuations of the 21 cm radiation arising from the hyperfine transition of neutral hydrogen. It is also aimed at measuring the baryon acoustic oscillations (BAO) from such fluctuations, thereby serving as a pathfinder to future, deeper intensity mapping surveys. The requirements for the Phase 1 of the projects consider a large reflector system (two 40 m-class dishes in a crossed-Dragone configuration) illuminating a focal plane with 28 horns to measure the sky, with two circular polarizations in a drift scan mode to produce measurements of the radiation in intensity (I) as well as the circular (V) polarization.

Aims. In this paper, we present the optical design for the instrument. We describe the optical arrangement of the horns in the focal plane to produce a homogeneous and well-sampled map after the end of Phase 1, as well as the intensity and polarization properties of the beams. Our analysis provides an optimal model for the location of the horns in the focal plane, producing a homogeneous and Nyquist-sampled map after the nominal survey time.

Methods. We used the GRASP package to model the focal plane arrangement and performed several optimization tasks to arrive at the current configuration, including an estimation of the sidelobes corresponding to the diffraction patterns of the two mirrors. The final model for the focal plane was defined through a combination of neural network and other direct optimization methods.

Results. We arrived at an optimal configuration for the optical system that includes the focal plane positioning and the beam behavior of the instrument. We present an estimate of the expected sidelobes both for intensity and polarization, as well as the effect of band averaging on the final sidelobes, as well as an estimation of the cross-polarization leakage for the final configuration.

Conclusions. We conclude that the chosen optical design meets the requirements for the project in terms of polarization purity and area coverage as well as a homogeneity of coverage so that BINGO can perform a successful BAO experiment. We further conclude that the requirements on the placement and rms error on the mirrors are also achievable so that a successful experiment can be conducted.

Key words. telescopes – radio lines: general – instrumentation: miscellaneous – cosmology: observations

1. Introduction

The Baryon Acoustic Oscillations from Integrated Neutral Gas Observations (BINGO) project is a two dish radio telescope[1] aiming to observe the 21 cm line corresponding to the hyperfine transition of neutral atomic hydrogen (HI). It will survey a sky area of ∼5324 square degrees (i.e., about 13% of the sky) in a redshift range spanning from 0.127–0.449 (corresponding to a frequency span of 980–1260 MHz).

Large-scale structure maps of the Universe have been made using optical galaxy spectroscopic surveys (Eisenstein et al. 2005; Beutler et al. 2011; Blake et al. 2011; Bautista et al. 2020; du Mas des Bourboux et al. 2020), however, only a small fraction of the Universe has been mapped with such techniques. It is clear that the advent of multi object spectrographs can assist the optical cosmologist in carrying out this task with greater efficiency (Levi et al. 2019). When we observe the sky in the radio part of the spectrum, we are able to map such spectroscopic information of the 21 cm line without having to specifically obtain the redshift of individual objects because we can obtain information at each frequency for the entire field. We obviously cannot identify each galaxy individually if the spatial resolution prevents us from doing so, however, we can directly obtain information about the redshifts of the galaxies present in the beam simply since there is minimal confusion between the 21 cm line and other emission in the radio part of the spectrum.

It has been proposed that mapping the Universe measuring the collective 21 cm line emission of the underlying matter (e.g., Madau et al. 1997; Battye et al. 2004) at low resolution may be much more efficient than doing so at higher resolutions or with optical spectrographs. This technique is called intensity mapping (IM; Peterson et al. 2009). The IM observation technique uses, in its most common realization, the 21 cm line emission line of HI, but possibilities of exercising this technique also exist using other lines, such as carbon monoxide lines (e.g., Lidz et al. 2011; Gong et al. 2012; Pullen et al. 2014). HI 21 cm line

[1] Although we have two dishes, the telescope works as a single dish radiometer, see Paper II of this series.

IM has been proposed as the main technique in several other projects such as MeerKAT (Santos et al. 2017), Tianlai (Chen 2012), CHIME (Bandura et al. 2014), HIRAX (Newburgh et al. 2016), and HERA (DeBoer et al. 2017), as well as SKA (Square Kilometre Array Cosmology Science Working Group 2020). The BINGO project will serve as an excellent opportunity to test IM performance in our redshift range. Details of IM and component separation approaches are described in two companion papers (Liccardo et al. 2021; Fornazier et al. 2021).

The BINGO telescope will measure HI in emission, the most common component present in our Universe. If we assume that the HI distribution follows the matter distribution in the Universe, we will be in a position to have a detailed map of the matter in intensity maps (Switzer et al. 2013). This will allow us to be the first experiment to measure the baryon acoustic oscillations (BAO) in the radio frequency band, although previous BAO detections have already been achieved in optical surveys (e.g., Eisenstein et al. 2005; Masui et al. 2013; Wolz et al. 2016, 2022).

The desired BAO signal depends on the width of the chosen bins in redshift and for binnings that correspond to around 0.05 in redshift (for an optimization of the binning width see Costa et al. 2022), this signal is on the order of a few hundred μK, more than 1000 times weaker than the smooth spectrum foreground signal. The relative strength of the foregrounds, which are partially linearly polarized and concentrated towards the Galactic plane, means that the observations need to be made with clean beam, low sidelobe levels and a very good level of polarization purity, to minimize RFI pick-up (Harper et al. 2018; Peel et al. 2019).

The need to resolve structures of angular sizes corresponding to a linear scale of around 150 Mpc in our chosen redshift range implies that the required angular resolution should be close to ∼40′ (Battye et al. 2013). The above requirements set out the primary scientific constraints to BINGO's optical design. The aim of this paper is to describe the steps that generate such a design, satisfying the requirements of the project in terms of polarization purity, beam shape, homogeneity of the covered area, and good sky sampling.

During Phase 1, the instrument should operate with 28 horns, a system temperature of $T_{\rm sys} \approx 70$ K per receiver and should be able to measure I and V polarization (Wuensche et al. 2022). The motivation of this paper is to describe the development of BINGO optical system relative to Phase 1. The BINGO project is described in Abdalla et al. (2022) and the current status of the project is presented in the companion papers (Abdalla et al. 2022; Wuensche et al. 2022; Liccardo et al. 2021; Fornazier et al. 2021; Zhang et al. 2022; Costa et al. 2022).

This paper describes the steps to produce the optical design that meets the BINGO scientific requirements. Section 2 contains a description of the optical design. Section 3 contains a study of the focal plane and description of the possible arrangements of horns in the focal plane. Section 4 sets out an optimization of the horn responses given their locations in the focal plane. Section 5 outlines the resulting beam profiles, projected beams for the scanning strategy and polarized responses as well as other properties of the optics chosen after optimization of the horn locations. We conclude our findings in Sect. 6.

2. BINGO optical design

2.1. Science requirements summary

Before embarking on an outline of the optical model definition, here we summarize the scientific requirements that are currently present in the literature. We discuss these requirements to a great extent throughout the manuscript; however, we set out an initial list here of the requirements already accepted in previous analyses (Battye et al. 2013). These requirements are summarized in Table 1.

Table 1. Requirements presented in Battye et al. (2013) for the BINGO telescope.

	Requirement	Value
(i)	Angular resolution	40 arcmin
(ii)	Operating frequency	960–1260 MHz
(iii)	Frequency resolution	≳1 MHz
(iv)	Frequency baseline as free as Possible from instrumental ripples	
(v)	Exceptionally stable receivers	
(vi)	Sky coverage	>2000 deg^2
(vii)	Number of feeds	>50
(viii)	Sidelobe levels as low as possible	
(ix)	Beam ellipticity	<0.1
(x)	No moving parts	
(xi)	Projected aperture diameter of the primary reflector	40 m
(xii)	Minimum number of pixels in the focal plane Each of them satisfying:	50
(xii) – (a)	Forward gain-loss in Comparison to central pixel	<1 dB
(xii) – (b)	Cross-polarization better than	−30 dB
(xii) – (c)	Beam ellipticity	<0.1
(xiii)	Focal length	90 m
(xiv)	Instantaneous field of view	10° × 9°

The operating frequency range is chosen such that we may avoid strong RFI from mobile phone downlinks. The current frequency interval is 980–1260 MHz and was chosen after the 2017 RFI campaign described in Peel et al. (2019). Stable receivers are a must to reach the required sensitivity of ∼100 μK per pixel, needed for BAO detection, and to minimize the nocive $1/f$ contribution to the system temperature, estimated to be $T_{\rm sys} = 70$ K. These and other instrument requirements are presented in a companion paper by Wuensche et al. (2022).

As explained in Battye et al. (2013), Fifty horns were shown to be an optimal number to achieve a good sensitivity for BAO detection. The setup discussed in this paper contains 28 horns in a different focal plane arrangement. This arrangement was tested in mission simulations and it delivers the required sensitivity, as discussed in the companion paper by Liccardo et al. (2021). Ultimately 28 horns will yield a less sensitive survey than the original 50 horns, however the simulations in this paper and the ones in Liccardo et al. (2021) show that this setup provides good enough results for the science to be achieved.

The low sidelobe requirement mentioned in (Battye et al. 2013) is expected to be achieved, since the measurements of the first sidelobes and beam shape of the prototype horn are well under −20 dBi and, in most of the frequency range, below −30 dBi. The beam symmetry is also well characterized in those measurements, as described in Wuensche et al. (2020). These low sidelobes are also needed to avoid ground pickup and RFI contamination from surface sources (mobile stations, ground radio links, etc).

The beam ellipticity shown in Table 1 would allow for map-making and power spectrum analysis routines to work efficiently.

A telescope with no moving parts would be stable, simple, and low-cost. An underilluminated primary reflector of 40 m is required in order to reach a resolution better than 40 arcmin at 1 GHz. The other requirements were reached after an extensive analysis presented in Sects. 3 and 5 of Battye et al. (2013), and the values presented in Table 1 serve as the baseline for this work.

2.2. Optical model definition

The current optical design for BINGO is based on a two mirror, off-axis, crossed Dragonian design (Dragone 1978; Tran et al. 2008), which is very common in CMB experiments because it minimizes cross polarization (e.g., Poidevin et al. 2018), so that the focal plane is at right angles to the incoming light, preserving the polarization of light. The primary mirror is a parabolic mirror with a focal length (f) of 140 m; the mirror is symmetric around its z axis and is a cut out of this parabola in the (x, y) plane centered at 226.54 m away from the origin with a diameter (D) of 40 m in this same (x, y) plane. This reference system will be called the global reference frame and the center of the primary is located at coordinates $(x = -226.54, y = 0, z = 91.64)$ m in this frame.

The secondary mirror is a hyperbolic mirror. The origin of this hyperbola is placed at the focus point of the parabola described in the last paragraph. Therefore, the origin of this hyperbola reference frame is localized at (0, 0, 140) m of the global reference frame and is rotated relatively to the global system by the following Euler angles: $(180°, 95°, 0)$.

These results imply that for the primary reflector, we have $f/D = 3.5$ and the angle between the main reflector axis and the secondary reflector axis is 85°. The ratio of the distances between the foci relative to the main reflector focal length is 1.8 and the sub reflector eccentricity is −1.7. This yields an effective focal length for the optical system of 63.20 m. This value is somewhat smaller than the baseline design discussed in the previous section, however, this difference makes for a more compact design, which is beneficial given the size of the focal plane is already relatively large. Figure 1 shows the projections of the primary and secondary dishes onto the global reference frame, where the black color represents primary reflector and gray color represents the secondary reflector with its values in relation to global system. Here, we do not include the origins and foci of the parabola and the hyperbola, since that this would prevent us from looking at the curvature of the mirrors when zooming in on this representation.

Finally, the last coordinate system we set out here defines the location of the focus of the entire system and, hence, the location of the central feedhorn. This feed reference frame is located at position (0, 0, 252) m of the secondary reference frame (the one defined to locate the hyperbolic mirror) and has a rotation of the following Euler angles: (0, 153.27°, 180°). This reference frame will be used later on when we optimize the location of each feed horn in our focal plane.

In the global reference frame, the optical system is designed to look towards the z direction, therefore rotating the z axis of the global reference frame to coincide with the vertical axis of the site will make the telescope point to the zenith. Since the site coordinates are (latitude: 7° 2′ 27.6″ S; longitude: 38° 16′ 4.8″ W), rotating the optical system by 7.95° southwards (i.e., in the negative direction of the global system x axis) will point the central horn of the optical system to $\delta = -15°$. This configuration is plotted in Fig. 2.

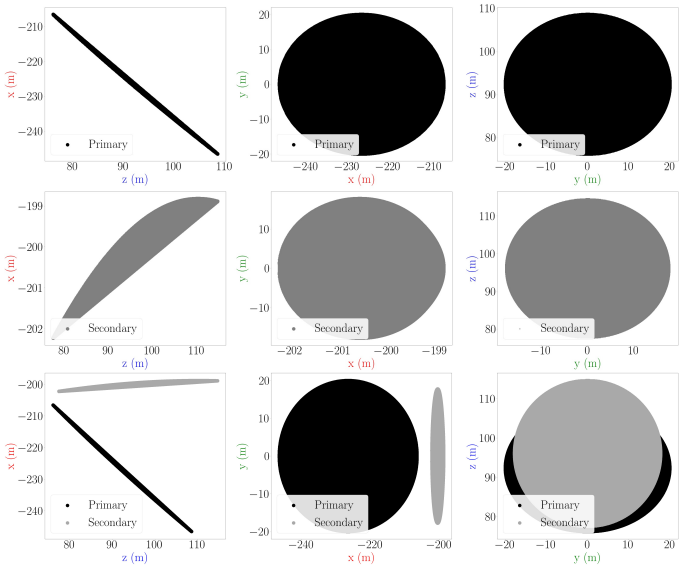

Fig. 1. Main and sub reflectors representations, in the global coordinate system and 2D-projections. *Top row*: primary reflector. *Left*: projection in the (x, z) plane. *Center*: Projection in the (x, y) plane. *Right*: projection in the (z, y) plane. *Center row*: secondary reflector. Left, center, and right are the same as in the top row. *Bottom row*: superposition of primary and secondary reflectors. Left, center, and right are the same as in the top row.

We implement the above optical configuration in the GRASP package (TICRA – Reflector Antenna and EM Modelling Software)[2] software to investigate four options of horn positioning in the focal plane to search for an optimal illumination and beam forming.

2.3. Optical arrangement implications for horn requirements

The theoretical design of the horns expect a return loss of ∼−40 dB across the band. A horn prototype has already been designed and fully tested. The results were reported by Wuensche et al. (2020) and the parameters described there are adopted for this study.

Together with the low sidelobe level (−27 dB below the peak for the first sidelobe), we require a spillover below 2% in order to satisfy our science requirements.

GRASP builds the simulation with the rays from horn to secondary reflector, and the rays reflected by it in direction of the main reflector. Therefore, for each reflector there will be an associated spillover. We use the labels "spillover1" to denote the secondary reflector and "spillover2" for the main reflector.

Since the field (in relation to the rays) contains the power expressed by Poynting's vector $\boldsymbol{S} = \frac{1}{2}\mathrm{Re}(\boldsymbol{E} \times \boldsymbol{H}^{\dagger})$, the power hitting a surface is:

$$W = -\int_{\mathcal{S}} \mathrm{d}\boldsymbol{a} \cdot \boldsymbol{S},$$

with $\mathcal{S}$ reflector surface. So, the spillover in the software is defined as:

$$spillover = 10 \log_{10} \frac{4\pi}{W}.$$

We used GRASP to model the optical configuration in later sections and derive an estimate for the spillover (see Sect. 5.2

[2] https://www.ticra.com/software/grasp/

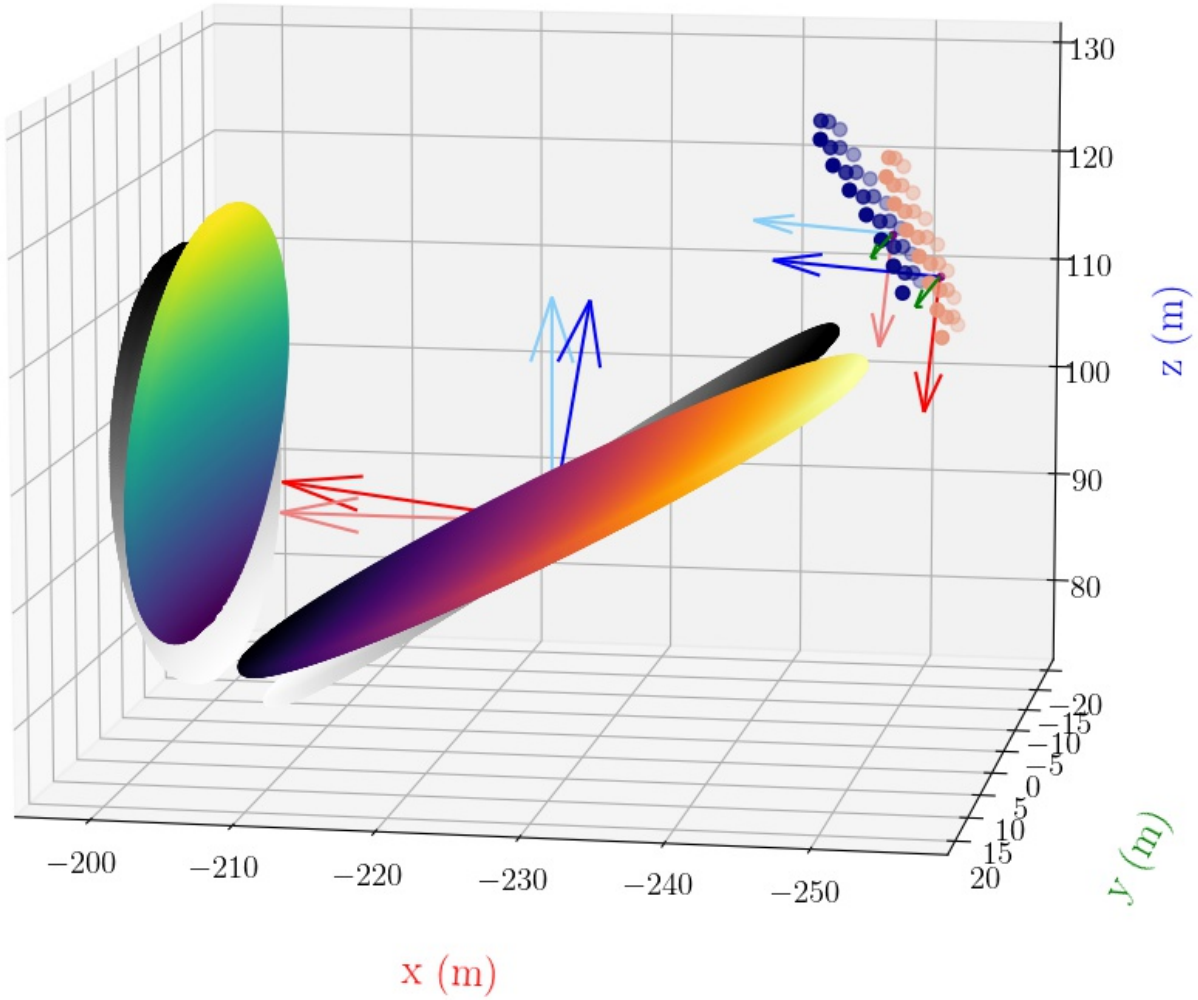

Fig. 2. 3D plotting of the optical system. The primary reflector in the center, the secondary reflector is on the left, and the horn array is on the right. The system is aligned in the north-south direction, with the secondary to the south and the horns to the north. The positions of the mirrors outlined in gray and black are in the global reference system; the colored position reflect the 7° rotation to account for the pointing of the telescope as described in the text. Horns plotted in salmon colors are in the optimal position.

for more comments) throughout the focal plane. These specifications determine the shape of the input response of the horn used in this paper, which is described in this next subsection.

2.4. Signal attenuation from horn design

The horns need to have very low sidelobes and the beam needs to be tapered so the illumination at the edge of the secondary mirror is less than −20 compared to the center, minimizing the spillover and ground pickup contributions to the incoming signal. In the resulting beam pattern, it is important for the faint HI signal to be efficiently separated from the bright Galactic foreground emission, whose signal is about four orders of magnitude brighter than HI.

In the optical system presented in Fig. 2, the half-angle subtended by the sub-reflector at the feed center is 17.98°. With a slight underillumination of the secondary, the resulting full width at half maximum (FWHM) for the whole telescope should be ≈40 arcmin (at the central frequency of our band), maintaining the original angular resolution requirements for the project.

This is mainly determined by the diffraction limit of the primary mirror but will of course depend on the details of the location of the horns and potential optical aberrations present in the system for horns which are not located at the exact focus of the telescope. Each horn in the focal plane will have a different full width half maximum (FWHM), which will be modeled and shown in Sect. 5. We also include images of the optical aberrations present in our focal plane given our configuration of choice.

In the analysis presented in this paper, we used the measurements of the horn radiation patterns reported in Wuensche et al. (2020) to produce fits to the measured horizontal (H) and vertical (V) polarization intensities used to model the full beam pattern of the telescope. The fits are shown in Appendix B. We compute the angle, and corresponding intensity values, for each frequency and each measured (V, H) intensity component, for which the intensity is attenuated by 10 dB and 20 dB in relation to the peak intensity. The results are show in Figs. 3 and 4 for the horizontal and vertical components, respectively. We stress here that we modeled the horns as Gaussian beams following the fits outlined above, as this are very good fits to the measurements presented in Wuensche et al. (2020); furthermore, we have neglected any cross coupling of the horns in this work. We also assume that the GRASP Gaussian beam is placed at the phase center of the physical horn which is located 30 cm inwards from the mouth of the horn.

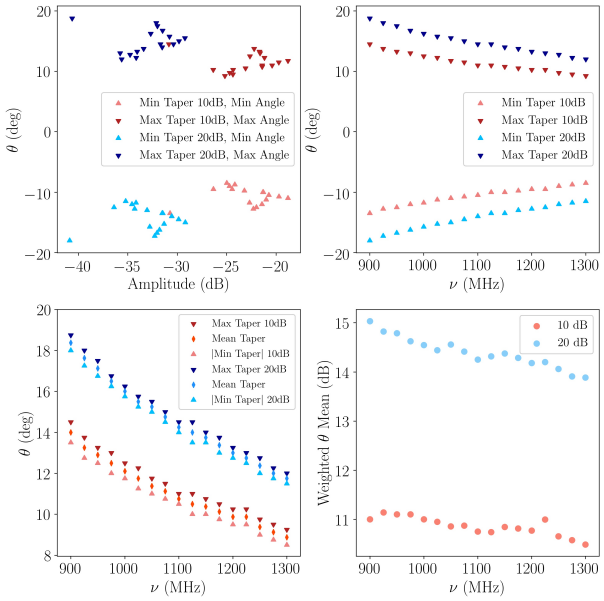

Fig. 3. Horizontal polarization intensity fits for the measurements of the prototype horn. *Upper left*: 10–20 dB attenuation angles values in different frequencies. *Upper right*: 10–20 dB attenuation angles × frequency. *Lower left*: attenuation angles absolute values. *Lower right*: 10–20 dB weighted attenuation angles × frequency. Minimum and maximum values are quoted in relation to maximum beam intensity for each frequency.

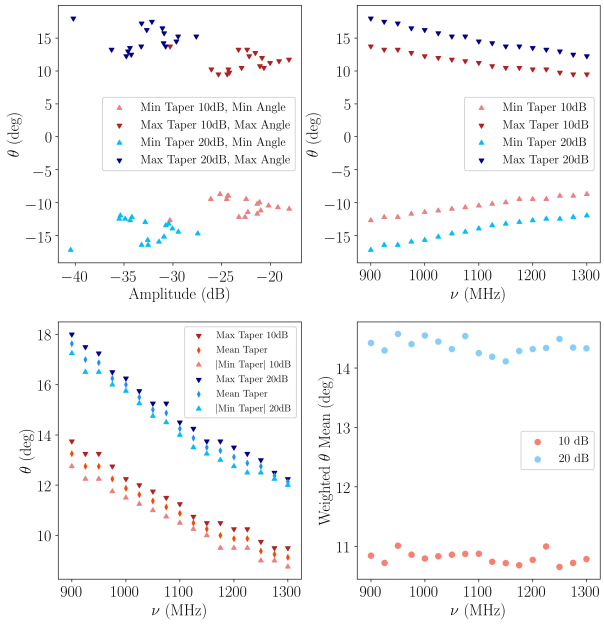

Fig. 4. Vertical polarization intensity fits for the measurements of the prototype horn. Legends are the same as for the horizontal measurements.

Figure 3 contains four plots: upper left show the angles for which the intensity is attenuated by 10 and 20 dB in relation to peak intensity, (hereafter, 10 and/or 20 dB attenuation angles). Upper right shows the 10 and 20 dB attenuation angles as a function of the frequency – we note the clear reduction of the angle opening as the frequency increases; lower left shows the maximum, mean, and minimum attenuation angles as a function of frequency, for 10 and 20 dB; lower right shows the weighted

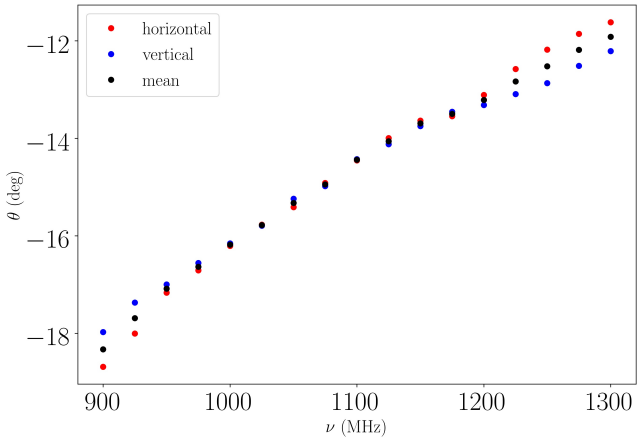

Fig. 5. θ attenuation angles values for vertical (*blue*) and horizontal (*red*) polarization intensity component in different frequencies and mean (*black*) value between both components in the same frequency.

average ($\theta \times \nu/(1000\,\mathrm{MHz})$ of the attenuation angles as a function of frequency. The same discussion applies to Fig. 4.

We used the 20 dB attenuation angles for both V and H components to compute mean values for each frequency and use the interpolations in this range in the GRASP simulations. The values shown in Fig. 5 are indeed smaller than the angle subtended by the sub-reflector at the feed center (17.98°) inside the 980–1260 MHz band. Hence, we confirm that our optical system is in fact under illuminated, producing the very low sidelobes as per the scientific requirements, as we show in subsequent sections of this paper.

3. Focal plane arrangements

The focal plane configurations studied for BINGO are shown in Fig. 6. For each configuration, we considered the following requirements: (a) homogeneous coverage of the sky; (b) sampling, in terms of elements of resolution per pixel, of the final maps (to be as close to Nyquist sampling, or better, if possible); (c) efficiency of the horns when placed at different locations of the focal plane.

Some original square configurations are not considered here. The collaboration generally considers the baseline configuration shown on the bottom-right arrangement shown in Fig. 6 (hereafter the hexagonal configuration). In this configuration, the horns are positioned in columns with different number of elements in relation to the central column, where a "central horn" pointing at $\delta = -15°$ is located.

The idea behind that original configuration is that there is a minimal amount of optical aberrations in the final beams, so that the beams are as clean and as close to Gaussian as possible (given that the horns are closely packed and as close to the focus as possible). The configuration is not a complete hexagon because the lowest horns would be obstructed by the primary mirror of the telescope and therefore cannot be considered. In this hexagonal positioning, the horns are encapsulated inside a regular hexagonal case.

However, we do have to consider that BINGO is a transit telescope with no moving reflectors. Therefore, as the sky drifts across the focal plane, it does so across the y direction of the focal plane, where the y coordinate has been taken to be the coordinate in the horn reference system, as plotted in Fig. 6. Therefore, each horn at a given x location would see the sky at a

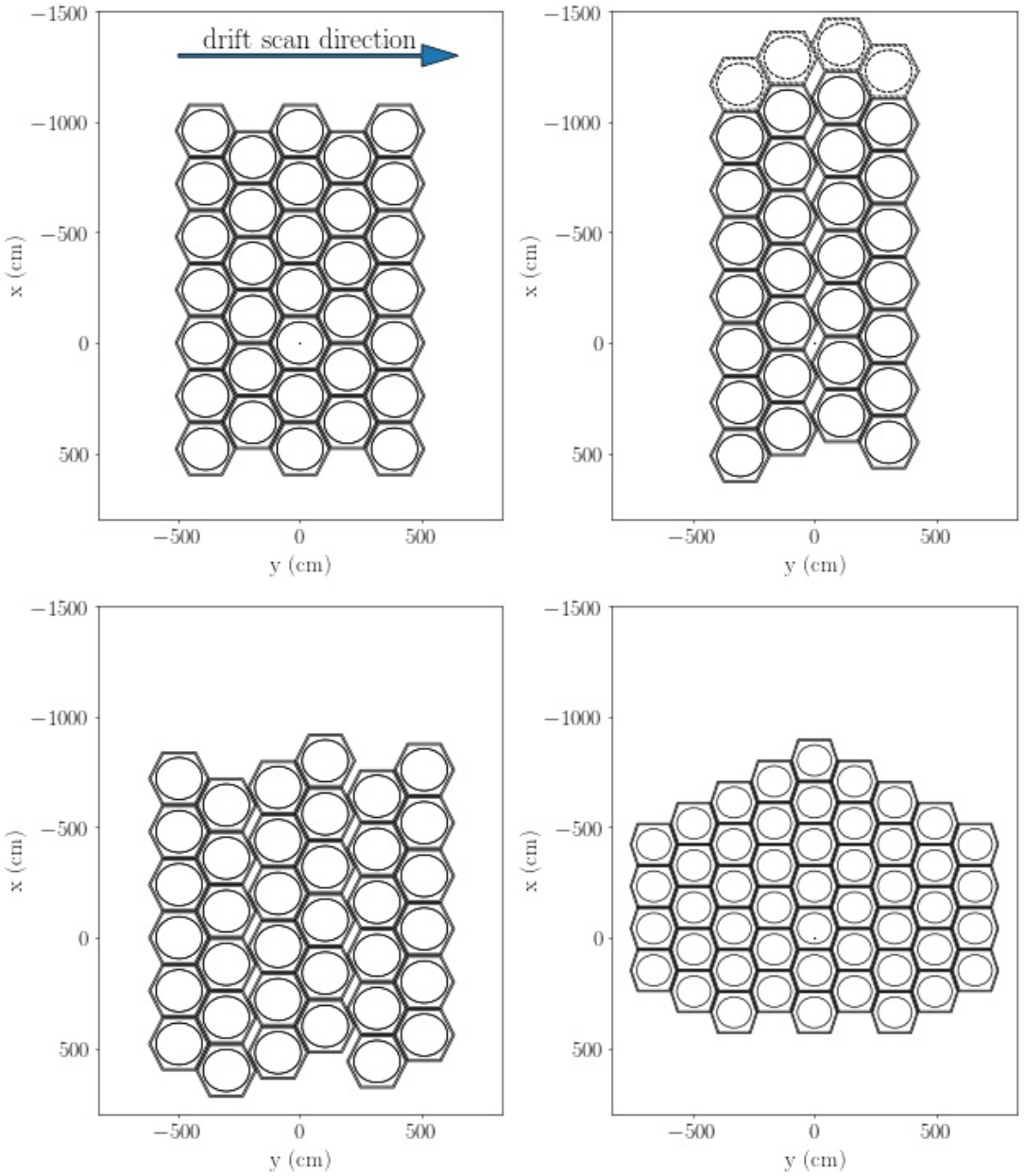

Fig. 6. Four focal plane arrangements studied in this paper, with different number of horns and different positions in the arrangement. *Top left*: rectangular. *Top right*: double-rectangular. *Bottom left*: triple-rectangular. *Bottom right*: hexagonal. In the three first arrangements, the hexagonal distribution (structure with the horn) has 249.44 cm as the maximum width and 240 cm as the height. In this structure, the circle represent central position of the horn with 190 cm in diameter. Arrangement four was built with different measures of the hexagonal structures to contain the horns, with 192 cm in maximum width and 190 cm in height. The arrow indicates the Bingo scanning direction in the sky.

given declination. If we look carefully at the hexagonal configuration, there are several horns that would see the sky at the same height, therefore at the same declination. This, in theory, would yield an uneven coverage of the sky (which is confirmed by our simulations in a latter section), which is less desirable when it comes to a power spectrum analysis of the underlying residual fields, which the 21-cm radiation will leave as an imprint.

The second issue with this hexagonal configuration comes about when we examine the number of pixels per resolution element for such horns. If we want to have a declination range of 15° in the sky, and also given that the focal length of the telescope is 63.2 m (as discussed previously) and the fact that the horns have a diameter of 1.9 m, this means that if the horns are closely packed, the beams would be separated by that ratio, which in degrees amounts to 1.73°. Therefore, even if we closely pack the horns in a vertical direction we would in fact undersample the focal plane of such an optical system.

If we want a 15° declination range, which is derived from the science requirements, and if horns of physical opening 1.9 m are separated in angular size by 1.73°, it means that our focal plane must be 16.49 high. We must note that the hexagonal distribution considered above would be just shy of this height. Therefore we started investigating other distributions that might deliver a better coverage in the desired declination range. If we then calculate the vertical separation needed for the beams to be separated by half a beam width, namely, their having a number of samples per beam equal to 2 (i.e., Nyquist sampled), we need to distribute the horns vertically every 37 cm; namely, 16.49 m divided by

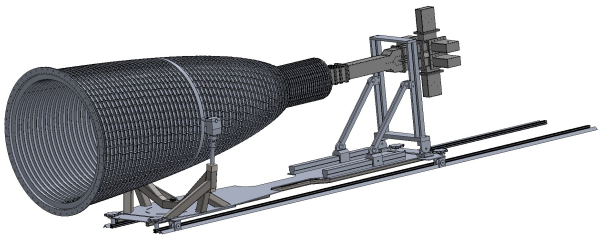

Fig. 7. Horn support system, designed to move the horn up and down according to the calculated positioning values. In the case of the double-rectangular and triple-rectangular the maximum value is ±30 cm from a central reference position. In the case of the rectangular arrangement, the value is ±42 cm. This cell support allows for the positioning of all horns in their optimal location as described in this paper. This is further discussed in the companion study in Paper (II) (Wuensche et al. 2022).

the number of resolution elements inside these 15°; that is, 15 divided by the beam size of two thirds of a degree times two to account for a Nyquist sampling.

The consequence of this is that in the hexagonal structure proposed as the fourth plot in Fig. 6, several horns would sweep the sky at the exact same declination (this would happen with horns which have same x coordinate). Assuming that the cells that hold the horns are hexagons of a height of 1.9 m, the adjacent horns would sweep in between gaps where the vertical separation would be 95 cm. This is a sampling which is significantly away from a Nyquist sampling of the focal plane calculated in the previous paragraph. We note here that one possible solution to this problem is to rotate the focal plane of the telescope appropriately, however this solution has been discarded, as it would increase the complexity of the structure that would be necessary to support the focal plane.

In order to solve for these two issues, we investigated three other arrangements, outlined in this same figure, and we discuss the benefits of each configuration in the remaining of this section. The three other configurations outlined in Fig. 6, called "rectangular" (top left), "double-rectangular" (top right), and "triple-rectangular" (bottom left) have larger cells, allowing the horns to be displaced upwards and downwards within the cell by up to 30 cm. The structure that encapsulates each horn is 2.4 m in height and, given their larger size, allows the original horn positions to be adjusted in the vertical position (referring to the encapsulating cell enclosure center) by ±15 and ±30 cm, changing the position each horn illuminates the secondary mirror. For the specific case of the rectangular arrangement, we used ±21 cm and ±42 cm for the shifts[3]. Figure 7 shows the mechanism where the horn is attached to the hexagonal case.

These three setups (displacements) allow for the necessary height adjustments to produce a very uniform sky coverage, in a slightly larger declination interval. In Fig. 6, there is no displacement, all horns are centered. With the extra height of the hexagons, we note from the figure that the focal plane for all three rectangular configurations is slightly greater than the 16 meters required in order for us to obtain a larger coverage than the 15° in declination. A full simulation of the integrated beams over right ascension is presented in Sect. 5 and we can indeed see that some of these configurations are more optimal than others.

In the double-rectangular configuration, two rows of detectors are shifted compared to the original first two rows of detectors by a one quarter height of the hexagon height. In other words, the height in the third and fourth rows of the double-rectangular array are shifted upwards from the first two columns by 60 cm. Given that the hexagonal configuration indicates that the difference in horn heights between the first and the second columns is half the hexagonal height, namely, 120 cm, we therefore have a configuration whereby each of the four horns cover the declination by being shifted by 60 cm steps in the x direction, as compared to one another. We can therefore reach a configuration that is better than a Nyquist configuration in this array by simply shifting the position of the horns once during the survey lifetime.

Should this be done each year of the survey, we can obtain a map that is oversampled in the x direction compared to Nyquist sampling, with the ability to explore the use of other techniques to extract further resolution from the maps, such as the drizzle technique used in the *Hubble* Space Telescope (Fruchter & Hook 2002). The triple-rectangular array is composed of more horns, composing a configuration that is possible in the case where it is possible to include more horns in the focal plane. It is similar to the double-rectangular arrangement, with the caveat that the columns are shifted by one third of the spacing between the hexagonal cells.

In the following sections, we make full simulations for the four arrangements shown in Fig. 6 to ensure that the horns are in optimal locations of the focal plane of the telescope. We show, using full electromagnetic simulations, the effects of the focal plane distribution as well as the implications of these choices on the beam shapes and polarization of the beam.

4. Optimization of the focal plane

Given that obtaining the best solution for all points in the focal plane is a long and time-consuming computational task, we outline here a fitting technique where we select points in the focal plane (not in relation to the positions of the four arrangements, but for points that cover all regions of interest that cover those arrangements), where we fully solve for the best possible locations and angles of the horns in the focal plane and then interpolate for this solution on top of the solved points for each horn position in our focal plane arrangements from the last section.

For all four models for the configuration of the horns tests were carried out in order to identify their best positioning both in rectangular coordinates (x, y, z) and in angular coordinates (θ, ϕ)[4]. Within all but the hexagonal arrangement, the horns can move up to 30 cm upwards and downwards in vertical coordinates on the focal plane. In the two arrangements described as double and triple-rectangular, we have no central horn. The double-rectangular one was simulated with 28 horns (7 for each column) but there is the possibility to extend this upwards with another 4 horns. In Fig. 6, these additional horns were represented by dashed lines.

We note here that we have optimized the horn locations and angles by looking at the maximum signal intensity that was generated by our simulations at a frequency of 1100 MHz (roughly at the center of our central frequency of 1120 MHz). However, the BINGO frequency coverage spams 980 MHz to 1260 MHz, so, although the optimization in this work was performed at this frequency, we also observed the behavior of the beams in other frequencies between 980 MHz and 1260 MHz. Given that we performed this optimization throughout the focal plane, this applied to all arrangements.

[3] You can access the notebook that created this configuration on this link.

[4] Parameters θ and ϕ describe the pointing of the feed, ψ describes the polarization direction.

Table 2. Fitting parameters in Eq. (1) used to compute the estimated coordinates via a non-linear least-squares fit.

	Fitting parameters		
	z (cm)	θ (deg)	ϕ (deg)
a	1.1 ± 4.2	1.6079 ± 0.0904	89.8 ± 3.69
b	−0.048 ± 0.013	−2.422e-03 ± 2.80e-04	2.183e-01 ± 1.14e-02
c	0.00e-03 ± 9.7e-03	0.00e-04 ± 2.11e-04	0.00e-03 ± 8.42e-03
d	0.00e-05 ± 1.7e-05	0.00e-07 ± 3.79e-07	0.00e-05 ± 1.54e-05
e	2.1e-04 ± 2.2e-05	9.747e-06 ± 4.82e-07	4.52e-05 ± 1.97e-05
f	7.6e-04 ± 4.0e-04	9.574e-06 ± 8.73e-07	−2.32e-05 ± 3.57e-05
g	0.00e-08 ± 2.8e-08	0.00e-10 ± 6.14e-10	0.00e-08 ± 2.40e-08
h	1.97e-07 ± 3.0e-08	4.8107e-09 ± 6.53e-10	−1.941e-07 ± 2.67e-08
i	3.9e-08 ± 6.7e-08	2.07e-09 ± 1.45e-09	−3.071e-07 ± 5.94e-08
j	0.00e-08 ± 3.0e-08	0.00e-10 ± 6.63e-10	0.00e-08 ± 2.67e-08
k	−1.08e-10 ± 6.1e-11	− 2.79e-12 ± 1.31e-12	−2.293e-10 ± 5.36e-11
l	5.4e-11 ± 9.4e-11	−4.10e-12 ± 2.02e-12	−2.56e-11 ± 8.27e-11
m	5e-05 ± 1.4e-04	−1.416e-05 ± 2.99e-06	−9.14e-04 ± 1.22e-04
n	−6.3e-05 ± 5.5e-05	− 1.92e-06 ± 1.19e-06	1.67e-05 ± 4.85e-05

In order to obtain the (z, θ, ϕ) positions for each horn achieving maximum intensity, we sought the values of these parameters that maximized $10\log_{10}(\|E_{\rm co}\|^2)$, using the TICRA-GRASP software. These parametric values are equivalent to the intensity itself[5]; the same is true for the Q polarization parameter. The first calibrations were made as follows: given a horn to be analyzed, identified by positions x and y, we looked for the value of the parameters (z, θ, ϕ) that provided the maximum amplitude, scanning all the possible values. This was done for a set of 52 (x, y) positions.

The data obtained by the above method made it possible to fit for a z as well as for a θ symmetry and a ϕ anti-symmetry with respect to y. We thus achieved a total of 96 positions for our parameter fits (all these 96 positions are obtained independently of the arrangements discussed). We searched analytic fits to represent $(\hat{z}, \hat{\theta}, \hat{\phi})$, for each (x, y) in the region of interest. It was possible to find good fits (regression model with non-linear least squares) for the angular parameters using only a polynomial as a function of x and y. We used the function $\hat{z}(x, y)$, $\hat{\theta}(x, y)$, $\hat{\phi}(x, y)$, defined as:

$$a + bx + cy + dxy + ex^2 + fy^2 + gx^2y + hxy^2 + ix^3 + jy^3 + kx^4 + ly^4 + \frac{m}{(x + 10^{-5})} + \frac{n}{(y + 10^{-5})}, \quad (1)$$

with coefficients from a to n presented in Table 2. We note that given we have performed the fits throughout the focal plane, the fits apply to all arrangements.

The z-fit required a more refined analysis to understand its lack of smoothness, with some positions appearing quite different from others. To analyze this region, with the calibrated values of the angular parameters, we carried out a complete analysis of how the amplitude varies with z. Taking the maximum intensity for $x > -400$ cm values generates a gradual evolution of the parameter, but not for $x < -400$ cm. The amplitude can be seen at different positions in Fig. 8 where each graph represents the amplitude with respect to z for a given y and x spaced by 50 cm, from −400 to −1000 cm. A table of the results for this optimization is given in Appendix A.

[5] The intensity is obtained by $10\log_{10}(\|E_{\rm co}\|^2 + \|E_{\rm cx}\|^2) \approx 10\log_{10}(\|E_{\rm co}\|^2)$ the peak position does not change either.

We note here that our optimization procedure creates an optical surface where the horns are to be placed. This optical surface has a small curvature, as can be seen in Fig. 2. This optimization leads to an optical surface that is continuous, positioning the horns in an optimal way. The horns are not expected to see each other much more than they would if placed side by side on a plane. However, we do not take into account the coupling between the horns when located in the optical surface. This is currently assumed to be small and will investigated in future modeling.

It is possible to see that for a given y, the peak at $x = -400$ cm, is not necessarily the highest peak. This fact is very clear in the graphs for $y = -350$, -400 and -450 cm. They could be a second or third peaks in the response curve, most likely due to different aberrations being more dominant, and for this reason it was not possible to achieve a monotonous representation of z, in the x and y plane, taking only the maximum amplitude values. To have a smooth representation and thus achieve a fit, it was necessary to restrict ourselves to the same peak for different xs and follow its modification in relation to x, for a given y. It is possible to see the depth of focus for all 13 settings above in Fig. 9 where we take the intensities at each selected peak and its respective z value called by $I_{\rm max}$ and $z_{\rm max}$, respectively; then, we find $\|z_{\rm max} - z\|$ where $\|I_{\rm max} - I\| = 0.005$ dBi and plot it in Fig. 9, where each line represents a fixed y value for variable x positions. We see that all z-values are in the range $6.5 \leq y \leq 11.5$ cm.

Thus, we obtained the z for these peaks in different xs, at the given y. Then we looked at a smooth function (Eq. (2)) that, for each y (and based on the results), we obtained the z value that would give us a smooth evolution. With these results, namely, by occasionally taking a secondary peak to ensure the smoothness of the function, z, we obtained the positions given in Table B.1 and Fig. 10. With this fit, we obtained a root mean square (rms) for the fit of the z position of below 12 cm,

$$\hat{z}_y(x) = a + bx + cx^2 + dx^3 + ex^4 + \frac{f}{(x + 10^{-5})} + \frac{g}{(x + 10^{-5})}. \quad (2)$$

The z-rms is 11.63 cm; for θ we found 0.25° and $\phi = 10.27°$. In Fig. 11, we can see the absolute difference between the calibrated values and those reconstructed in each position.

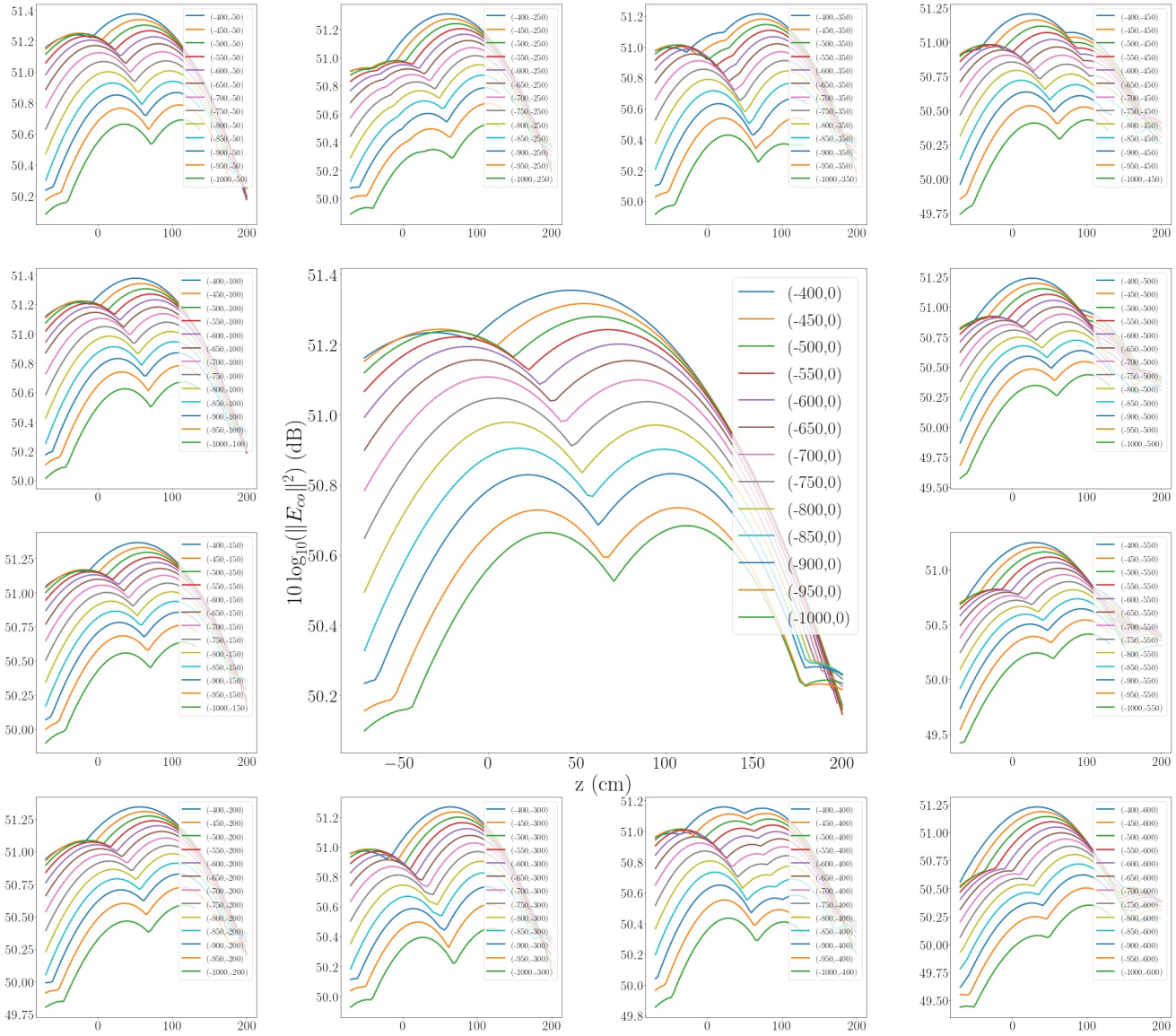

Fig. 8. Evaluation of z parameter in relation to x coordinate for different y coordinates. The x values are between -1000 and -400 cm with 50 cm intervals for all plots. The y values are between -600 and 0 cm, starting in upper left plot and finishing in lower right plot. These values corresponds to critical region in focal plane for z parameters to obtain the fit.

We also built a dense neural network (DNN) to reconstruct the parameters z, θ, and ϕ. Thus we built three DNN, using the data obtained by the GRASP simulations. For the three parameters, we chose a DNN with ten neurons. First, we divided our dataset into train and test sets, where this division is random to avoid overfitting. The division was 70% train and 30% test. We also did the standardization by removing the mean and scaling to unit variance.

Because of the size of the dataset, we made the choice to run 300 DNN realizations. We then averaged the outputs for all of our realizations. For each realization, it was required for the neural network to take 20 000 minimization steps to fit our parameters.

The fitting of the z parameter was chosen using the x and y as inputs. Therefore, given the position in x and y, we can predict z; thus, within the training, we achieved the predicted values given by the DNN. Performing this fitting process with several different DNN for the parameters θ and ϕ yields slightly different results. After the training was performed, we computed the rms of our realization over all 300 DNNs, which is provided in Table 3[6].

Finally, we showed the results obtained by DNN and the non-linear least-squares model, which are summarized in Figs. 10, 11, 12, and 13[7]. The above two fits define the best locations for the horns to be placed in the focal plane, which is indeed not a plane but a complex two-dimensional (2D) curved surface that we outlined earlier in this section. For the subsequent calculations presented in this paper, we used a non-linear least-squares fit.

5. Results

5.1. Beam analysis

In this section, we describe the computation of the beam profiles for each arrangement we have previously considered. We

[6] That calculation can be seen on this notebook link
[7] The results applied to all the arrangements in this article studied can be accessed on this notebook link

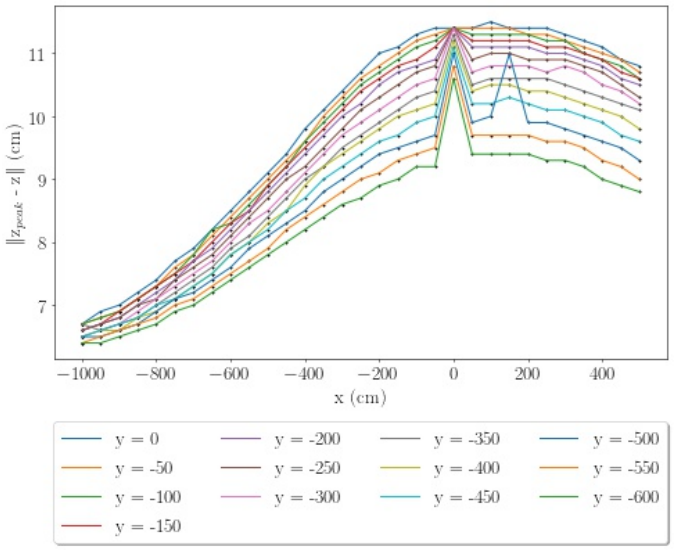

Fig. 9. Each depth of focus curve required for appropriate focusing of the horn, considering a defocusing of 0.005 dBi for 13 different y positions.

Table 3. Rms of the coordinates computed in Table 2 for the non-linear least-squares fit and DNN fits.

Parameter	Non-linear LS	DNN
z (cm)	11.63	10.21
θ (deg)	0.25	0.68
ϕ (deg)	10.27	7.89

used the GRASP software for any horn of any given arrangement where each one is defined by their standard rectangular and angular coordinates, both of which have been computed and interpolated using the previously described least-squares fitting of the optical surface. GRASP propagates a monochromatic, Gaussian, and linearly polarized beam through the optical system, and provides the response as a 2D complex electrical field in u–v coordinates over the sphere. We chose, however, to present the results in celestial coordinates (RA, Dec) selected at a given specific time of the survey (specified as any time when RA of zero is located directly south), given that BINGO is a transit telescope. For this purpose, we performed a linear interpolation of the data according to the sequence of transformation defined below. First of all, we transformed (u, v) to standard Cartesian coordinates (x, y, z) on the unit sphere:

$$x = u, \tag{3}$$

$$y = v, \tag{4}$$

$$z = \sqrt{1 - u^2 - v^2}. \tag{5}$$

The u–v coordinates can be understood as a plane tangent to the sphere on the center of the beam, which is at $x = y = 0$ and $z = 1$ in this system. In order to transform to celestial coordinates, however, it is helpful to define a new Cartesian system such that the z-axis points to the celestial north pole. We choose to rotate the center of the focal plane to be located at declination $-15°$ of the celestial equatorial plane, therefore we are required to perform a rotation of 105° (i.e., 90° + 15°) from the celestial

Table 4. FWHM (deg) of beams computed in Fig. 15.

0.633	0.611	0.615
0.601	0.592	0.607
0.620	0.632	0.619
0.711	0.671	0.663

pole, which is where GRASP was set up to produce our beam:

$$\begin{pmatrix} x' \\ y' \\ z' \end{pmatrix} = \begin{pmatrix} \cos 105° & 0 & \sin 105° \\ 0 & 1 & 0 \\ -\sin 105° & 0 & \cos 105° \end{pmatrix} \begin{pmatrix} x \\ y \\ z \end{pmatrix}, \tag{6}$$

and the definitions of the Celestial coordinates follow in a straightforward fashion:

$$\mathrm{Dec} = \arcsin(z'), \tag{7}$$

$$\mathrm{RA} = \arctan2(y', x') = 2\arctan\left(\frac{y'}{\sqrt{(x'^2 + y'^2)} + x'}\right). \tag{8}$$

Figure 14 shows the response due to the BINGO central horn only. The quantity being plotted is the intensity $I_{\mathrm{dB}} = 10\log_{10}(I)$, where the intensity I (in W) is defined by the sum of squares of the two orthogonal components of the electrical field:

$$I = |E_{\mathrm{co}}|^2 + |E_{\mathrm{cx}}|^2, \tag{9}$$

where E_{co} is the electric field measured in linear polarization and E_{cx} is the electric field measured in cross-polarization. For the single horn analysis, the number of points, N_{p}, for writing the fields outputs of the GRASP software was chosen to be 1614×1614 in a (u, v) range from -0.7 to 0.7. We further compute the average of the intensities from each linearly polarized beam.

Figure 15 shows the optical aberrations for the beams of a hypothetical focal plane, with the central horn located at the focus of the telescope, which points at $\delta = -15°$. Due to the horn arrangement, the boresight is always at a declination $\delta < \delta_{\mathrm{center}}$. Nevertheless, we can see that the beam shape is relatively well behaved across this hypothetical focal plane, and that the aberrations remain at a level below 30 dB, at (RA, Dec) $\lesssim |0.67|°$ from the center of the main beam. This gives us the confidence that the optical aberrations within the field of view chosen by this work can be modeled well when the final survey is produced. Table 4 shows the FWHM values for the beams presented in Fig. 15. Values are listed in the same order as beams in the figure. We also calculated the ellipticity, defined as $e = \sqrt{1 - ((FWHM_x)/(FWHM_y))^2}$ for a set of five horns located at several locations in the focal plane at positions (x, y) : $((0, 0), (450, 304), (510, -304), (-930, -304), (-990, 304))$. In all sets, the calculated ellipticity values ϵ are smaller than 0.1, meeting the requirements published in Battye et al. (2012).

Furthermore, for the sake of comparing the different configurations, we computed all the beams of each configuration for frequencies of 980 MHz, 1100 MHz, and 1260 MHz, and accurately setting the attenuation angle according to the method previously explained in Sect. 2.4. Also, we averaged the response of each linearly polarized beam. We recall that although we present the results in (RA, Dec) coordinates, the originally simulations were made in (u, v) coordinates. We chose range in (u, v) coordinates for the simulations is from -0.2 to 0.2 for the hexagonal and rectangular arrangements, with 461×461 points,

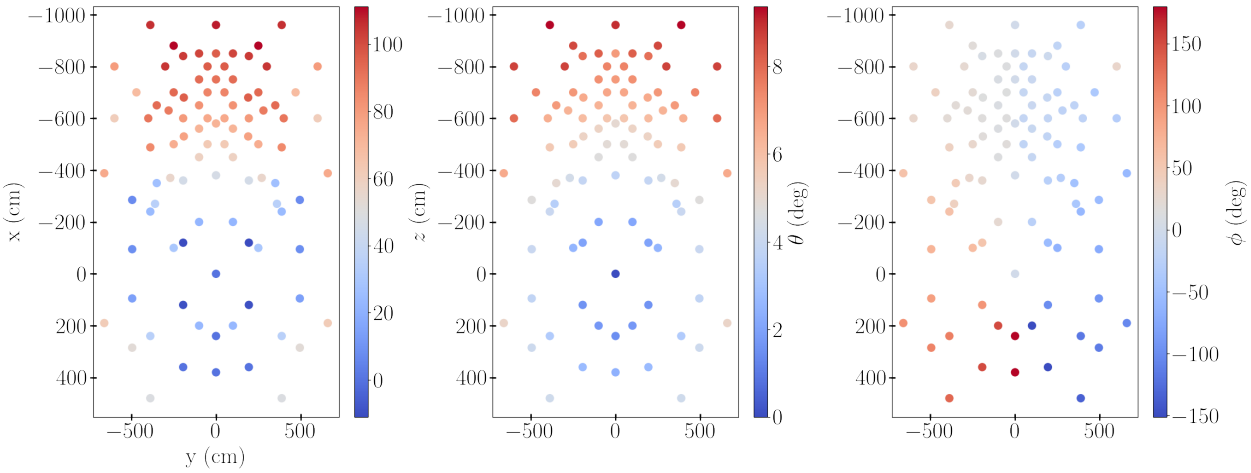

Fig. 10. Optimized horns parameters with GRASP only using the same peak in z range in relation to the x coordinate. The vertical axis of the plots are x values in cm and horizontal axis, y in cm.

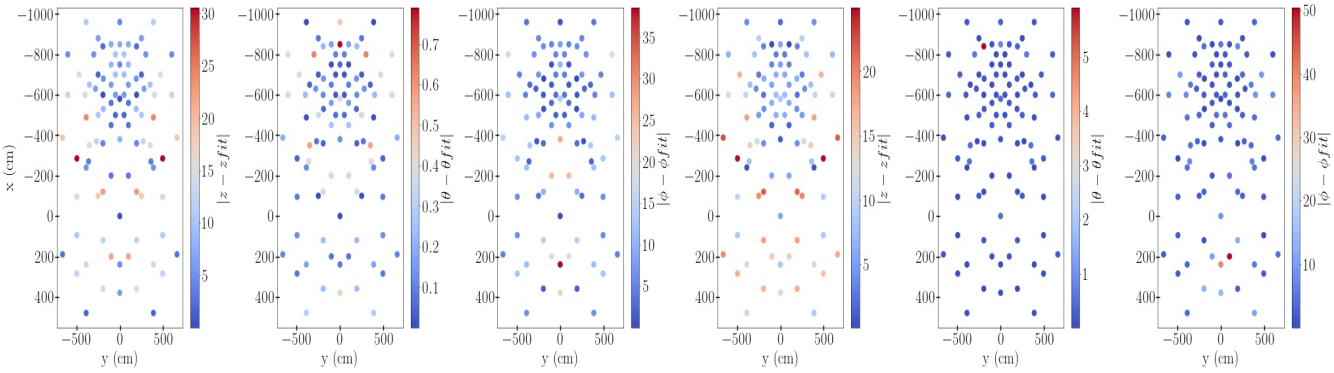

Fig. 11. Comparison between parameters optimized and estimated by non-linear least-squares and dense neural network fits. *Left*: absolute difference between calibrated parameter values and fitting parameters. The first plot is the difference for the z parameter, the center plot is the difference for the θ parameter, and the last plot for ϕ. The fit used was that of Eq. (1) with values in Table 2. The vertical axis of the plots are x values in cm and horizontal axis, y in cm. *Right*: same analysis, but with a fit computed by a DNN.

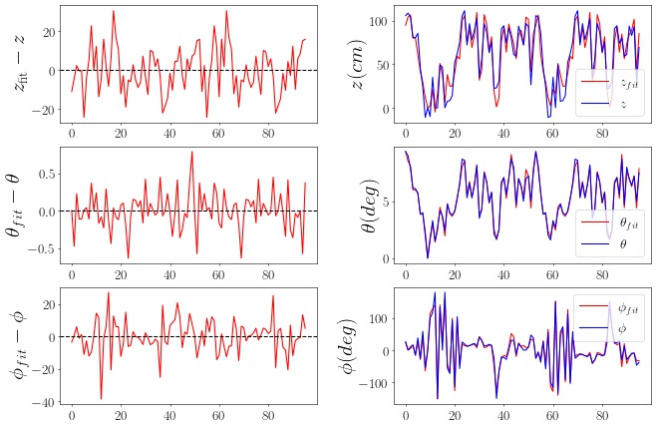

Fig. 12. Non-linear least-squares fitting for every 96 positions on the focal plane for each estimated coordinate. The *left column* shows the difference between estimated and optimized parameters, and the *right column* shows estimated and optimized views together.

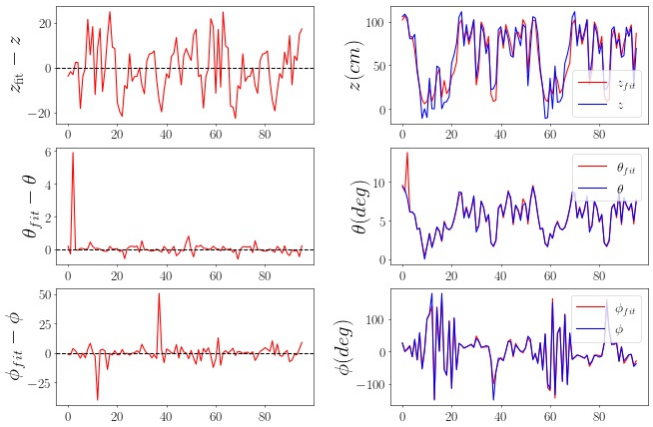

Fig. 13. DNN fitting for every 96 positions on the focal plane for each estimated coordinate. The *left column* shows the difference between estimated and optimized parameters, and the *right column* shows estimated and optimized views together.

and from −0.4 to 0.4 for the double-rectangular and triple-rectangular arrangements with 922×922 points. Then, although the simulated area is not the same, we maintained a resolution of 1152.5^2 points per unit of area, which has been shown to be good enough for the interpolation procedure. Moreover, we defined a total intensity for the arrangement, normalized by the intensity peak of the central horn, according to:

$$p^{\nu}_{\rm arr}(\mathrm{RA}, \mathrm{Dec}) = \frac{\sum^{\rm horn} I^{\nu}_{\rm horn}(\mathrm{RA}, \mathrm{Dec})}{I^{1100\,\mathrm{MHz}}(0, -15^{\circ})} \quad (10)$$

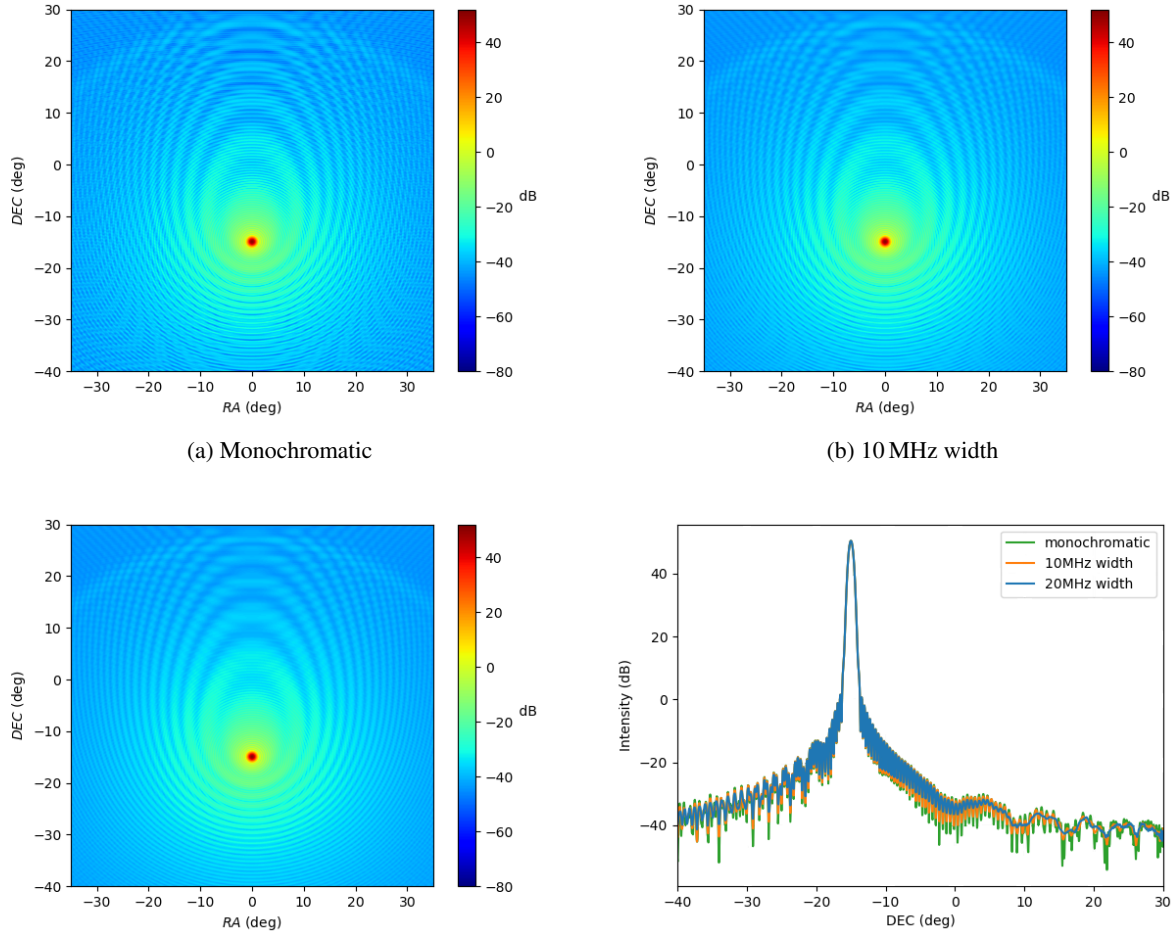

(a) Monochromatic

(b) 10 MHz width

(c) 20 MHz width

(d) 1-D

Fig. 14. Sidelobes of the BINGO central beam present a Moirré effect due the two-mirror configuration of the instrument (panel a). We found that this effect is attenuated when integrating the beam. Panels b and c show integrated beams over widths of 10 MHz and 20 MHz respectively, computed in the range 1105–1115 MHz and 1100–1120 MHz, with displacements of 1 MHz and normalized by the number of steps. The attenuation effect is clearer in panel d, portraying a 1D cut of the results from panels a–c.

and its one-dimensional version as well:

$$P^{\nu}_{\rm arr}(\,{\rm Dec}) = f \times \frac{\int {\rm dRA}\ \sum^{\rm horn} I^{\nu}_{\rm horn}({\rm RA}, {\rm Dec})}{\int {\rm dRA}\ I^{1100\,{\rm MHz}}({\rm RA}, -15^{\circ})}, \tag{11}$$

where the RA dependence is removed by integration.

The results of applying Eq. (10) to the double-rectangular, triple-rectangular, rectangular, and hexagonal arrangements are shown in Fig. 16, while the results of applying Eq. (11) are depicted in Fig. 17. Unless stated otherwise, all results were computed at $f = 1100$ MHz. Although the sum in Eq. (10) is over all horns, in Eq. (11), for the rectangular and hexagonal arrangement, the selection covers the central column of horns and also one adjacent. For the double and triple-rectangular, however, we select all the columns, since its particular geometry does not create overlaps. For this reason, in Eq. (11) we set $f = 1/2$ for the double-rectangular, $f = 1/3$ for the triple-rectangular, and $f = 1$ for the rectangular and hexagonal, since for the double (and triple)-rectangular, the beams are summed up over twice (and triple) the numbers of columns. This has been chosen so that the contents of Fig. 17 reflect the integrated beam while the sky swipes across the focal plane.

We stress here that we have interpreted the results of the double-rectangular distribution as the best results given that the smoothness of the coverage would indicate that the noise properties of the final map are as close to homogeneous as possible. If the maps were not Nyquist-sampled and the resulting projected beam along the declination direction was not smooth, we would obtain a map with noise properties that exhibit a pattern on the sky. This is clearly undesirable when it comes to performing a power spectrum analysis of the residuals, as we would have to model this inhomogeneity perfectly in order to obtain results about the power spectrum of 21 cm radiation. Therefore, the smoother versions of such an arrangement are preferred over the non-smooth versions. An analysis of the impact of this on the power spectrum of the final datasets presented in our companion paper (Liccardo et al. 2021).

Additionally, the results presented in the Fig. 17 were averaged over the five displacements of $0, \pm 15$ cm, ± 30 cm for the double-rectangular and triple-rectangular and $0, \pm 21$ cm, ± 42 cm for the rectangular arrangement. This is done so that the final coverage of the focal plane is optimal with respect to the Nyquist theorem, as outlined in Sect. 3. This averaging produces a smoother intensity profile for those three arrangements as compared to the hexagonal arrangement which is not averaged. Also, the double and triple-rectangular present even smoother profiles compared to the rectangular arrangement, which can be explained by the particular geometry of the arrangements. We

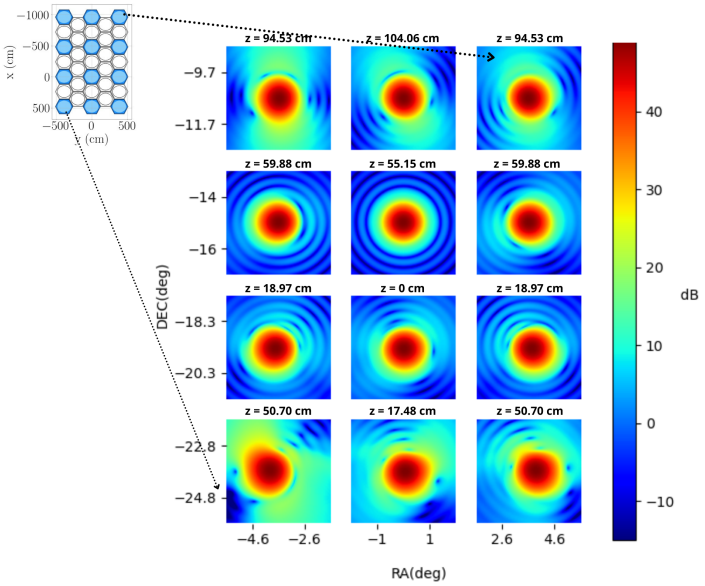

Fig. 15. Optical aberrations for the final beams of the horns located at different places within the focal plane (corresponding locations x and y chosen according to upper left figure and the respective z values over each horn, in the focal plane localization). The focus of the telescope is placed at $\delta = -15°$ and has a beam that is devoid of aberrations while the aberrations are increasingly large, but less than ∼10 dB, as we move away from the center of the focal plane.

conclude that this smoothness will most likely lead to a sky coverage that avoids gaps in the coverage, which is confirmed in our companion paper (Liccardo et al. 2021). We conclude here that the configuration that best achieves smoothness with the minimum number of horns is the double-rectangular and is the configuration that we adopted as the standard configuration for the project.

5.1.1. Beam polarization

We investigated the polarization properties in this section by computing the four Stokes parameters for each beam and summing them up for each arrangement. We applied the following definition:

$$I = |E_{\rm co}|^2 + |E_{\rm cx}|^2 = |E_{\rm a}|^2 + |E_{\rm b}|^2 = |E_{\rm rhc}|^2 + |E_{\rm lhc}|^2, \quad (12)$$

$$Q = |E_{\rm co}|^2 - |E_{\rm cx}|^2, \quad (13)$$

$$U = |E_{\rm a}|^2 - |E_{\rm b}|^2, \quad (14)$$

$$V = |E_{\rm rhc}|^2 - |E_{\rm lhc}|^2, \quad (15)$$

where the subscripts refer to three different basis of the space of Jones vectors. With $(E_{\rm co}, E_{\rm cx})$ as the standard Cartesian basis (defined above), $E_{\rm a}$ and $E_{\rm b}$ are defined by a rotation of the Cartesian basis used to define $(E_{\rm co}, E_{\rm cx})$, rotated by 45°, and with $E_{\rm rhc}$ and $E_{\rm lhc}$ as the left-handed and right-handed basis, respectively, defined as follows:

$$e_{\rm a/b} = \frac{1}{\sqrt{2}}(\pm e_{\rm co} + e_{\rm cx}), \quad (16)$$

$$e_{\rm lhc/rhc} = \frac{1}{\sqrt{2}}(e_{\rm co} \pm i e_{\rm cx}). \quad (17)$$

The polarized responses of the beam present either positive or negative Q values around 20 dB below the gain of the unpolarized I beam when averaged over RA. The levels of U polarization

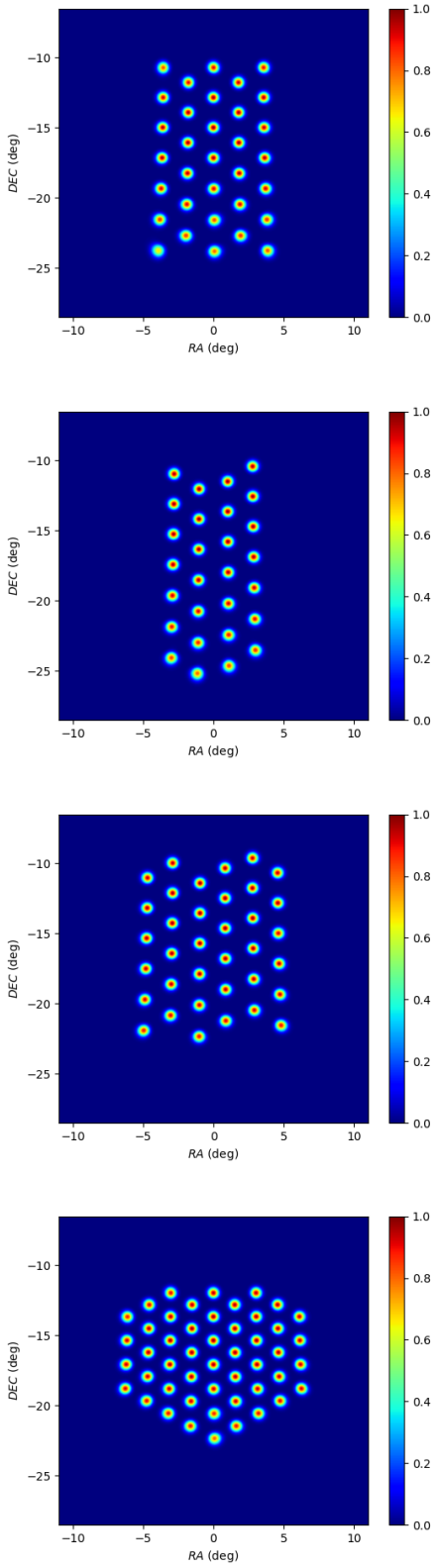

Fig. 16. Beam responses (intensities, *from top to bottom*) for: (a) rectangular, (b) double-rectangular, (c) triple-rectangular and (d) hexagonal normalized by the intensity of the central horn (see Eq. (10)).

of the beam are a further five to ten orders of magnitude below this, depending on the position on the focal plane. We aimed to simulate the polarization gained through the optical system by an originally unpolarized beam, and assuming the input signal is

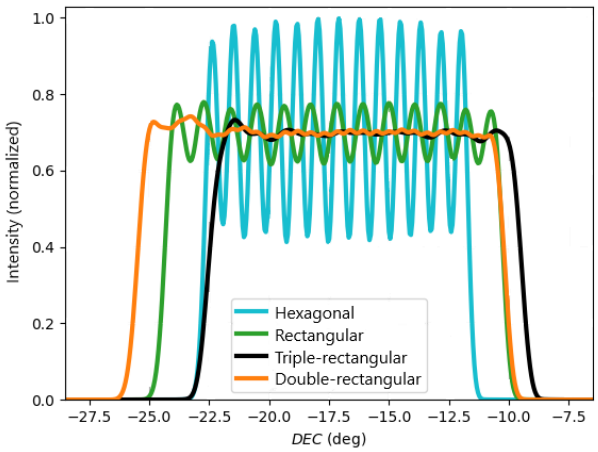

Fig. 17. Response function of the beams, integrated in RA, for selected columns (corresponding to a declination range) and different horn arrangements. Results are normalized to the response of the central horn, according to Eq. (11). For the triple-rectangular and double-rectangular arrangements, the beam average also took into account the five displacements of 0, ±15 cm, ±30 cm. For the rectangular arrangement, the five displacements were 0, ±21 cm, ±42 cm. This averaging produces an even smoother profile for the arrangements. We note that it is possible to change the orientation of the above figures on the sky by changing the north-south orientation of the telescope but maintaining the same boresight. This configuration was chosen in order have a simpler structure for the support of the mirrors and horns.

unpolarized, we averaged the response of both orthogonal polarized beams. While Q and U are highly dependent on these initial states, the I and V values are nearly the same for the two linearly polarized states. Despite this, this method enables us to subtract any effect that is due to the initial state of polarization.

The results for the Stokes parameters for the double-rectangular arrangement are shown in Fig. 18, along with a 1D cut in Fig. 19. Each parameter is summed up for all the beams of the configuration, computed in the frequency of 1100 MHz. Of course Q, U, and V are allowed to be either positive or negative, and the variation in their sign reveals a balance between the field directions. It is also instructive compare the magnitude of the parameters. In Fig. 19, we see that V is at least 25 dB lower than I in the peaks and the difference is even higher for the Q and U parameters. We note here that the results in Fig. 18 represent the response of unpolarized point sources located where each of the horns are pointing in the sky, therefore representing the optical contribution from the leakage coming from the arrangement, including that coming from the sidelobes. However, it neglects any other potential leakage that might be included in the rest of the instrument, including the electronics.

5.1.2. Beam window function

In this section, we compute the power spectra for the beams to investigate the effect it will have in modifying the final power spectrum of the 21 cm radiation that we are studying. It is important to estimate this as any strong features in the beam window function could be misinterpreted by a measured feature in the 21 cm power spectrum.

In order to compute the beam spectra, our first step was converted our data to `HEALPix` format. We linearly interpolated the values of intensity of each beam from the original u–v coordinates to the coordinates of the centers of the pixels of a `HEALPix` pixelated sphere with $N_{\rm side} = 1024$. This $N_{\rm side}$ value was set in order to make the new resolution compatible with that of our GRASP simulations. We also set to zero the intensity outside the area where the simulations were performed since it is expected to be very low away from the beam center. Afterwards, we computed the projections in harmonic space and all the angular power spectra with a `PseudoPower` code (Loureiro et al. 2019). The intensities of each map were previously normalized by its sum over the pixels. The spectra for the beams of the double-rectangular arrangement are shown in Fig. 20 for the frequencies of 980 MHz, 1100 MHz, and 1260 MHz. We see that these spectra reach lower values in high-ℓ for lower frequencies. In the same figure, we can infer the effect due to the horn location over the arrangements. This reflects the aberrations of the beams when displaced away from the center of the optical plane (Fig. 15).

We conclude that the beams are smooth enough and concentrated enough so as to not produce any significant effects in the measurements of the power spectrum of the 21 cm at the angular scales relevant to BINGO. Furthermore, such a modeling procedure can be used in order to produce a more realistic fit to the beams for the purposes of map-making, although due to the underillumination of the secondary mirror, the beams are very close to Gaussian in the center of the field.

5.2. Spillover

The telescope design is set up in such a way that the secondary mirror is underilluminated by the horns given the combination of the focal length chosen and the angular aperture of the horns. As such the spillover of this setup is extremely low at the boresight of the telescope, which is the horn that will point at declination $\delta = -15^\circ$ and is located at position $(x, y) = (0, 0)$.

We need to assess if the optical arrangement, which requires the horns to point to a given location in the focal plane, has a spillover that is significantly different for each of the horns located outside the main focus of the telescope. In Fig. 21, we plot the calculated spillover, which is expected given the optical arrangement of the telescope as well as the shape proposed by the focal plane after the optimization performed in this paper. We can see that at the focus of the telescope the spillover is very low at around 0.003 dB (lowest value on the scale in Fig. 21). Figure 21 shows us the spillover more than doubles in dB at the edges of the considered focal plane, however, even at the locations furthest from the center of the focal plane, it remains at a value lower than 0.007 dB.

The above results are encouraging, as they mean that even without shielding of the main mirror and without any further measures to avoid ground pickup, the spillover for the entire system should remain below 0.007 dB and in most cases, around 0.003–0.004 dB. We are considering using a ground shield around the primary and at the bottom of the secondary dish, which should considerably improve the above values.

6. Conclusions

This work presents the focal surface calculation as well as a detailed description of the analysis conducted to produce the optical arrangement for the BINGO telescope.

Our target was to arrive at a cross-Dragone configuration that was under-illuminated, with very low cross-polarization leakage and sidelobe levels. For each horn, the attenuation obtained from our simulations is better than 60 dB a few degrees away from the center of the beam, which is crucial to obtain data that

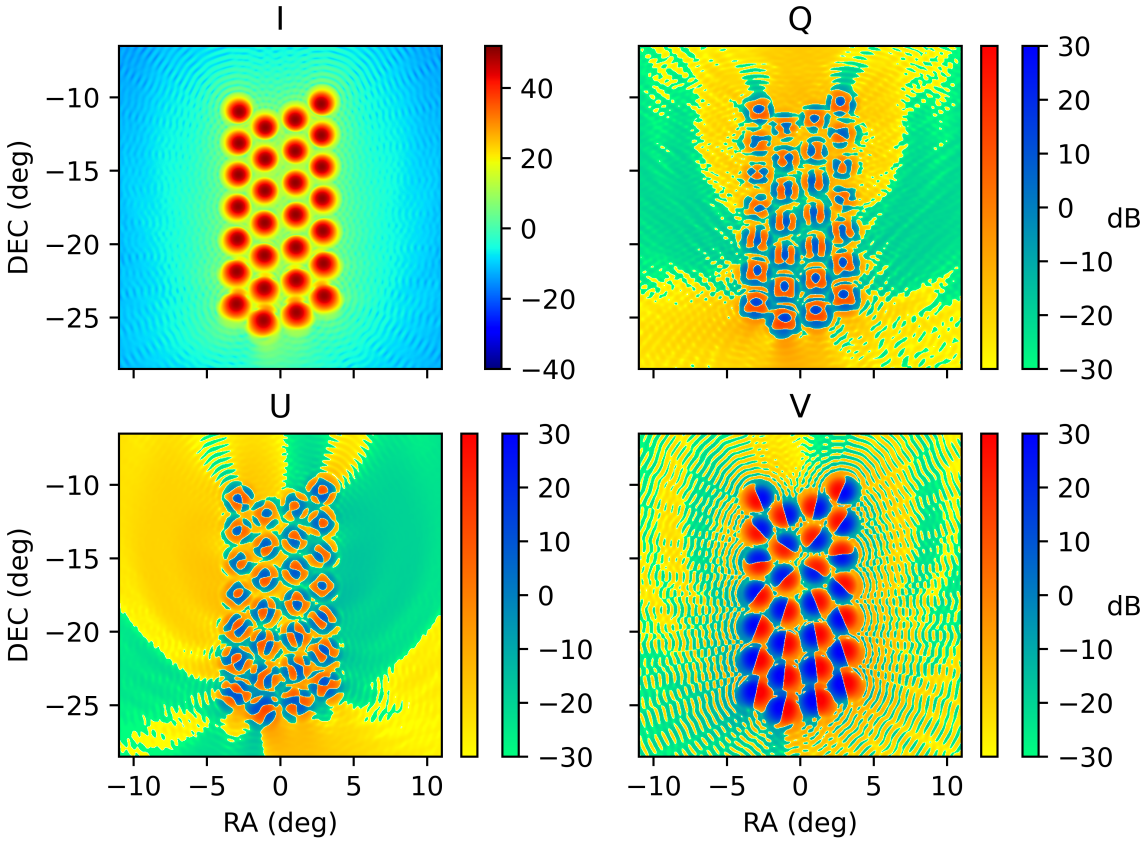

Fig. 18. Stokes parameters I, Q, U, V summed up for the beams of the double-rectangular arrangement and transformed to dB units, namely, $X_{\rm dB} = 10\log_{10}(\pm X)$. The two color bars indicate the positive (red) and negative (blue) values for the Q, U and V parameters. Each beam was previously averaged between the responses of each linearly polarized state.

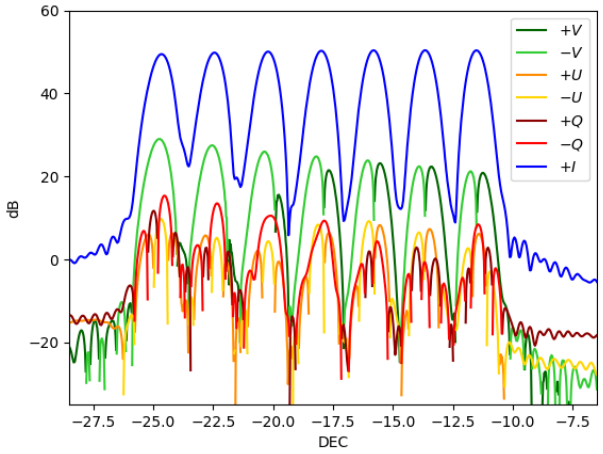

Fig. 19. 1D cut of the Stokes parameters presented in Fig. 18 for the double-rectangular arrangement. The cut is over $\mathrm{RA} = \mathrm{RA}_{\rm peak}$, where $\mathrm{RA}_{\rm peak}$ is the coordinate of the peak in intensity. We see that V is at least 25 dB lower than I on the peaks, while Q and U are even lower.

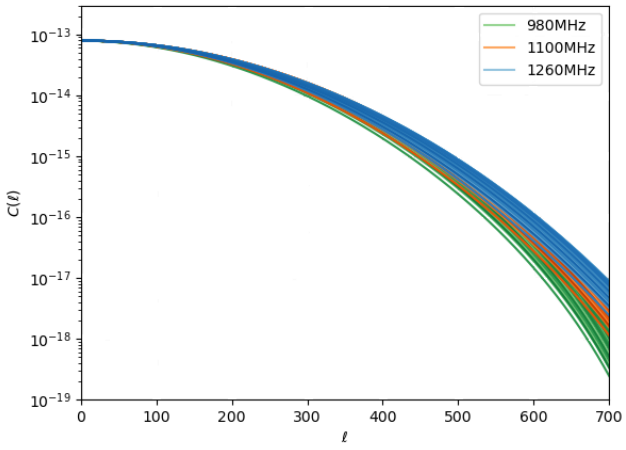

Fig. 20. Auto-angular power spectra for the double-rectangular arrangement beams. We computed the spectrum for each one of the 28 horns of the arrangement for the frequencies of 980 MHz, 1100 MHz and 1260 MHz. We can see that low frequencies have lower power at high multipoles. The curves with similar shades of color correspond to the same frequency but different horns, so the reader can also see the affect due to the location in the optical plane. The intensities were previously normalized with respect to the integral over the simulated area yielding to an adimensional spectrum (with no units), which also represents the window function of the eventual survey.

is robust with regard to sidelobe contamination, especially for observations performed near the Galactic center.

The polarization leakage in the Stokes parameters U and V is attenuated by ≈25 dB, compared to the I intensity in the beam across the field of view. These results indicate that the proposed configuration is appropriate for the scientific goals of BINGO.

We also analyzed the shape and orientation of the focal plane of this cross Dragone configuration. We found a non-planar focal surface with a complex shape, mainly due to the fact that multiple local maxima are present when optimizing the location, as well as the angular orientation of the horns away from the focus

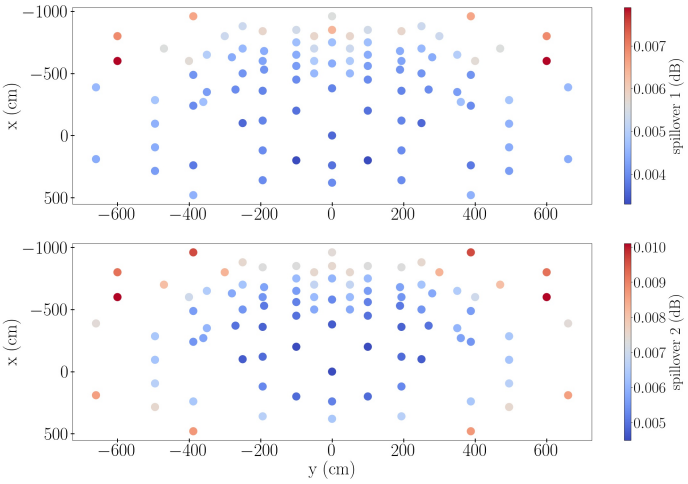

Fig. 21. GRASP's spillovers of every 96 positions with optimized coordinates. *Top*: Spillover1 is in relation to the secondary reflector. We can see that at the focus of the telescope the spillover1 is 0.0036 dB and that at worst it is raised to 0.008 dB at the edges of the focal plane. *Bottom*: Spillover2 is in relation to the primary reflector. Its spillover at the center is 0.0045 dB and the worst is 0.0101 dB.

of the telescope. This lead us to find specific local maxima of the peak response of the field as a function of the horn positions (most specifically, the z direction defined in the frame of the horns) in order to have a suitably shaped focal plane. Given the focal length coupled with the size of the horns, the Nyquist properties of the focal plane were investigated. A suitable shape for the focal surface was found in order to optimize the coverage of the final survey.

The level of optical aberrations was investigated for detectors away from the focus of the instrument. One of our first commissioning tasks will be to compare the measured beam patterns with the simulated ones. We find that for the double-rectangular array, the optical aberrations are acceptable and only modify the beam at the level of the sidelobes a couple of degrees away from the main peak beam. Furthermore, we find that the attenuation of the main peak of the beam is maintained at reasonable levels, namely, at the edge of the chosen field the attenuation is at most 0.5 dB and is maintained within a fraction of a dB_i in most places inside the focal surface.

To maintain a focus tolerance of 0.005 dB, we find that the depth of field for our focal surface should be ∼10 cm. This is in agreement with the mechanical tolerances and requirements of the engineering project designed to host the focal surface, as well as the noise budget from the full BINGO detection system. We have checked that for several positions within our focal plane, our ellipticity requirement of 0.1 is satisfied and this is indeed the case for the optical design proposed. Furthermore we have checked that the cross Dragone design used in BINGO Phase 1 achieves a polarization purity of −30 dB as demanded by scientific requirements and this is the case for most of the focal plane, as can be seen from Fig. 19. The only place where the requirements are close possibly below the simulation is at declination $\delta = -25°$, where the V polarization gets to −25 dBi from the peak response of the I polarization. On the other hand, U and Q Stokes parameters are well below the −30 dBi benchmark, as required for polarization purity.

We ultimately arrived at an optimal configuration, denoted as the double-rectangular, which meets the requirements for the scientific performance of the instrument. This arrangement, coupled to a system that allows the vertical displacement of the horns in subsequent years of the survey allows for a homogeneous and gap-free coverage of the sky. The simulations indicate a low spillover and good beam performance. In summary, according to the results presented here, the double-rectangular arrangement is considered the nominal configuration for the Phase 1 survey.

Acknowledgements. The BINGO project is supported by FAPESP grant 2014/07885-0; the support from CNPq is also gratefully acknowledged (E.A.). F.B.A. acknowledges the UKRI-FAPESP grant 2019/05687-0, and FAPESP and USP for Visiting Professor Fellowships where this work has been developed. We thank Edvaldo Barbosa Guimarães Filho for his help and support in relation to codes and optimizations. K.S.F.F. would like to thank FAPESP for grant 2017/21570-0. C.A.W. acknowledges a CNPq grant 2014/313.597. T.V. acknowledges CNPq Grant 308876/2014-8. E.J.M. acknowledges the support by CAPES. A.A.C. acknowledges financial support from the China Postdoctoral Science Foundation, grant number 2020M671611. B.W. and A.A.C. were also supported by the key project of NNSFC under grant 11835009. V.L. acknowledges the postdoctoral FAPESP grant 2018/02026-0. C.P.N. thanks São Paulo Research Foundation (FAPESP) for financial support through grant 2019/06040-0. M.P. acknowledges funding from a FAPESP Young Investigator fellowship, grant 2015/19936-1. R.G.L. thanks CAPES (process 88881.162206/2017-01) and the Alexander von Humboldt Foundation for the financial support. A.R.Q., F.A.B., L.B., and M.V.S. acknowledge PRONEX/CNPq/FAPESQ-PB (Grant no. 165/2018). L.S. is supported by the National Key R&D Program of China (2020YFC2201600). J.Z. was supported by IBS under the project code, IBS-R018-D1.

References

Abdalla, E., Ferreira, E. G. M., Landim, R. G., et al. 2022, A&A, 664, A14 (Paper I)
Bandura, K., Addison, G. E., Amiri, M., et al. 2014, SPIE Conf. Ser., 9145, 914522
Battye, R. A., Davies, R. D., & Weller, J. 2004, MNRAS, 355, 1339
Battye, R. A., Brown, M. L., Browne, I. W. A., et al. 2012, ArXiv e-prints, [arXiv:1209.1041]
Battye, R. A., Browne, I. W. A., Dickinson, C., et al. 2013, MNRAS, 434, 1239
Bautista, J. E., Paviot, R., Magaña, M. V., et al. 2020, MNRAS, 500, 736
Beutler, F., Blake, C., Colless, M., et al. 2011, MNRAS, 416, 3017
Blake, C., Davis, T., Poole, G. B., et al. 2011, MNRAS, 415, 2892
Chen, X. 2012, in International Journal of Modern Physics Conference Series, 12, 256
Costa, A. A., Landim, R., Novaes, C., et al. 2022, A&A, 664, A20 (Paper VII)
DeBoer, D. R., Parsons, A. R., Aguirre, J. E., et al. 2017, PASP, 129, 045001
Dragone, C. 1978, AT T Tech. J., 57, 2663
du Mas des Bourboux, H., Rich, J., Font-Ribera, A., et al. 2020, ApJ, 901, 153
Eisenstein, D. J., Zehavi, I., Hogg, D. W., et al. 2005, ApJ, 633, 560
Fornazier, K. S. F., Abdalla, F. B., Remazeilles, M., et al. 2022, A&A, 664, A18 (Paper V)
Fruchter, A. S., & Hook, R. N. 2002, PASP, 114, 144
Gong, Y., Cooray, A., Silva, M., et al. 2012, ApJ, 745, 49
Harper, S. E., Dickinson, C., Battye, R. A., et al. 2018, MNRAS, 478, 2416
Levi, M., Allen, L. E., Raichoor, A., et al. 2019, Bull. Am. Astron. Soc., 51, 57
Liccardo, V., de Mericia, E. J., Wuensche, C. A., et al. 2022, A&A, 664, A17 (Paper IV)
Lidz, A., Furlanetto, S. R., Oh, S. P., et al. 2011, ApJ, 741, 70
Loureiro, A., Moraes, B., Abdalla, F. B., et al. 2019, MNRAS, 485, 326
Madau, P., Meiksin, A., & Rees, M. J. 1997, ApJ, 475, 429
Masui, K. W., Switzer, E. R., Banavar, N., et al. 2013, ApJ, 763, L20
Newburgh, L. B., Bandura, K., Bucher, M. A., et al. 2016, SPIE Conf. Ser., 9906, 99065X
Peel, M. W., Wuensche, C. A., Abdalla, E., et al. 2019, J. Astron. Instrum., 8, 1940005
Peterson, J. B., Aleksan, R., Ansari, R., et al. 2009, in astro2010: The Astronomy and Astrophysics Decadal Survey, 2010, 234
Poidevin, F., Rubino-Martin, J. A., Genova-Santos, R., et al. 2018, ArXiv e-prints, [arXiv:1802.04594]
Pullen, A. R., Doré, O., & Bock, J. 2014, ApJ, 786, 111
Santos, M. G., Cluver, M., Hilton, M., et al. 2017, ArXiv e-prints, [arXiv:1709.06099]

Square Kilometre Array Cosmology Science Working Group (Bacon, D. J. et al.) 2020, PASA, 37, e007
Switzer, E. R., Masui, K. W., Bandura, K., et al. 2013, MNRAS, 434, L46
Tran, H., Lee, A., Hanany, S., Milligan, M., & Renbarger, T. 2008, Appl. Opt., 47, 103
Wolz, L., Blake, C., Abdalla, F. B., et al. 2016, MNRAS, 464, 4938
Wolz, L., Pourtsidou, A., Masui, K. W., et al. 2022, MNRAS, 510, 3495
Wuensche, C. A., Reitano, L., Peel, M. W., et al. 2020, Ex. Astron., 50, 125
Wuensche, C. A., Villela, T., Abdalla, E., et al. 2022, A&A, 664, A15 (Paper II)
Zhang, J., Motta, P., Novaes, C., et al. 2022, A&A, 664, A19 (Paper VI)

[1] Department of Physics and Astronomy, University College London, Gower Street, London WC1E 6BT, UK
e-mail: filipe.abdalla@gmail.com
[2] Instituto de Física, Universidade de São Paulo, C.P. 66318, CEP: 05315-970, São Paulo, Brazil
e-mail: alessandro.marins@usp.br; pablo.motta@usp.br
[3] Instituto Nacional de Pesquisas Espaciais, Divisão de Astrofísica, Av. dos Astronautas, 1758, 12227-010 São José dos Campos, SP, Brazil
[4] Department of Physics and Electronics, Rhodes University, PO Box 94, Grahamstown 6140, South Africa
[5] Laboratoire Astroparticule et Cosmologie (APC), CNRS/IN2P3, Université Paris Diderot, 75205 Paris Cedex 13, France
[6] IRFU, CEA, Université Paris Saclay, 91191 Gif-sur-Yvette, France
[7] Department of Astronomy, School of Physical Sciences, University of Science and Technology of China, Hefei, Anhui 230026, PR China
[8] Institut d'Astrophysique Spatiale, Orsay (CNRS-INSU), France
[9] Unidade Acadêmica de Física, Univ. Federal de Campina Grande, R. Aprígio Veloso, 58429-900 Campina Grande, Brazil
[10] Instituto de Física, Universidade de Brasília, Brasília, DF, Brazil
[11] Centro de Gestão e Estudos Estratégicos – CGEE, SCS Quadra 9, Lote C, Torre C S/N Salas 401–405, 70308-200 Brasília, DF, Brazil
[12] Center for Gravitation and Cosmology, College of Physical Science and Technology, Yangzhou University, Yangzhou 225009, PR China
[13] School of Aeronautics and Astronautics, Shanghai Jiao Tong University, Shanghai 200240, PR China
[14] Max-Planck-Institut für Astrophysik, Karl-Schwarzschild Str. 1, 85741 Garching, Germany
[15] Technische Universität München, Physik-Department T70, James-Franck-Straβe 1, 85748 Garching, Germany
[16] Instituto de Astrofísica de Canarias, 38200 La Laguna, Tenerife, Canary Islands, Spain
[17] Departamento de Astrofísica, Universidad de La Laguna (ULL), 38206 La Laguna, Tenerife, Spain
[18] Center for Theoretical Physics of the Universe, Institute for Basic Science (IBS), Daejeon 34126, Korea

Appendix A: GRASP setup

We can divide the GRASP calculation process used here into four steps: (1) obtain currents (*Get Current*) with a specific feed as source and the sub-reflector (hyperbolic dish) as the target; (2) obtain currents (*Get Current*) using sub-reflector as source and main reflector (parabolic dish) as the target; (3) calculate the field (*Get Field*) using the main reflector as source; and (4) calculate the field (*Add Field*) using a feed as source. The currents calculation using *PO Analysis*[8] also use PTD[9] correction, that is, we used PO+PTD currents. PTD corresponding to currents from the edges of the reflector. The PO+PTD need of three parameters (po1, po2 and ptd) to calculate to convergence of the currents calculations and provided by auto-convergence (established **ON**). Those parameters are estimated by the geometry of the optical system and by the chosen wavelength. Tables A.1 and A.2 show examples of values chosen for parameter calculation. For these cases we chose five different positions (P0, P1, P2, P3, P4) in the focal plane to display the values. We assumed the GRASP standard value for field accuracy (-80 dB in relation to the peak). The third and fourth steps build the spherical grid file in calculating the field. Spherical grid files (Section 4) were configured into a UV grid, both x-range and y-range, with: start = -0.5, end = 0.5 and np = 151[10]. Rectangular truncation and linear polarization were established as default.

Appendix B: Calibrated horn parameters

We chose random positions on the focal plane to able to obtain the fit for parameters z, θ, and ϕ from x and y coordinates. We using the symmetries of the focal plane to obtain more calibrated values. The lines with Modified equal True are the positions where we used the symmetry from ϕ, as previously described. In Table B.1, we present all the values used in this paper.

Appendix C: Horn attenuation angle

We interpolate the beam data (horn response) and built two sets of data, for each beam component and each frequency, with intensity decrease value of 10 and 20 dB in relation to maximum intensity value (first lobe) and we take the corresponding angle values, as can seen in figure C.1 for horizontal component of the beam and in figure C.2 for vertical one. In figure C.1, we can see the main results separated by correlation between maximum and minimum angles, frequency, and amplitude of the intensity. The first and third plots in the first row are relations between minimum and maximum angles with its amplitude value for horizontal and vertical component, respectively. Salmon and red colors are related to decrease in intensity of 10 dB for minimum and maximum angle, respectively, and light blue and navy blue for 20 dB. Each color represent a group and is basically nested in the same region, but there is a more distant triangle for each group that are values from 900 MHz, where we have a first lobule with greater amplitude and wider (see Figures C.1 and C.2). Those can also be seen in the plots between frequency and angle (second and fourth plots in the first row). We can also see in those plots that the higher frequency, the lower the angles that delimit the peak interval. In the second row, first and third plots relate frequency and absolute angle, for minimum and maximum angle value, and its mean angle. The absolute value decreases with increasing frequency. Second and fourth plots are the mean weighted values given by

$$\theta_{\rm weighted}(\nu) = \frac{\nu\ ({\rm MHz})}{1100\ ({\rm MHz})}\theta(\nu)\,, \tag{C.1}$$

where the decreases are smooth. Using a range between minimum and maximum angles, we fit the Gaussian function to the peak in order to estimate the 10-20 dB attenuation angles for the BINGO horn as a function of frequency. The results are fitted with the following function

$$G(\theta|a,b,c,d) = ae^{-0.5\frac{(\theta-b)^2}{c^2}} + d, \tag{C.2}$$

for both, 10 and 20 dB. We center the Gaussian beam in $b = 0°$ and take the new angles for 10 and 20 dB intensity decreases and each frequency. The results for 10 dB are shown in figure 5. Then, the attenuation angles were obtained by fitting the following:

$$\theta_{\rm taper}(\nu|a,b,c,d,f) = a + b\nu + c\nu^2 + \frac{d}{\nu} + \frac{f}{\nu^2}\,. \tag{C.3}$$

[8] PO = Physical Optics
[9] PTD = Physical Theory of Diffraction
[10] The choice of partial sky coverage does not change spillover values neither their respective intensities, as long as the beam in the sky is covered. However, changing np values can change the accuracy in the intensity determination.

Table A.1: Main parameters for convergence information for current calculations - feed as source and subreflector as target

Task 1 - Get Currents										
	x (cm)	y (cm)	z (cm)	θ (deg)	ϕ (deg)	po1	po2	ptd	po target	ptd target
P0	0	0	0	0.00	0.00	170	570	570	62350	570
P1	-990	305	98	9.28	-11.19	185	640	640	76082	640
P2	510	-305	45	4.08	145.08	160	540	530	55616	530
P3	-930	-305	102	8.98	15.77	185	630	630	74918	630
P4	450	305	36	3.62	-149.32	165	540	540	57365	540

Table A.2: Main parameters for convergence information for current calculations - subreflector as source, main reflector as target

Task 2 - Get Currents											
	x (cm)	y (cm)	z (cm)	θ (deg)	ϕ (deg)	po1	po2	ptd	po target	po source	ptd source
P0	0	0	0	-0.00	0.00	305	940	940	183690	62350	570
P1	-990	305	98	9.28	-11.19	305	900	860	175929	76082	640
P2	510	-305	45	4.08	145.08	305	980	980	191462	55616	530
P3	-930	-305	102	8.98	15.77	305	900	860	175929	74918	630
P4	450	305	36	3.62	-149.32	305	980	980	191462	57365	540

Table A.3: Main parameters for calculations of the field in the main reflector

Task 3 - Get Fields								
	x	y	z	θ	ϕ	field points	po source	ptd source
P0	0	0	0	-0.00	0.00	22801	183690	940
P1	-990	305	98	9.28	-11.19	22801	175929	860
P2	510	-305	45	4.08	145.08	22801	191462	980
P3	-930	-305	102	8.98	15.77	22801	175929	860
P4	450	305	36	3.62	-149.32	22801	191462	980

Table A.4: Main parameters for calculations of the field from the feed

Task 4 - Add Fields								
	x	y	z	θ	ϕ	field points	po source	ptd source
P0	0	0	0	-0.00	0.00	22801	62350	570
P1	-990	305	98	9.28	-11.19	22801	76082	640
P2	510	-305	45	4.08	145.08	22801	55616	530
P3	-930	-305	102	8.98	15.77	22801	74918	630
P4	450	305	36	3.62	-149.32	22801	57365	540

Table B.1: Calibrated horn positions and angles obtained using TICRA-GRASP.

Calibrated positions						
x (cm)	y (cm)	z (cm)[a]	θ (deg)[a]	ϕ (deg)[a]	Amplitude (dB)	Modified[b]
-960	-388	$105.5^{+0.1}_{-1.3}$	$9.37^{+0.25}_{-0.02}$	$26.30^{+1.21}_{-0.96}$	50.47	True
-960	0	$108.4^{+0.4}_{-0.7}$	$9.00^{+0.20}_{-0.10}$	$0.00^{+2.63}_{-2.63}$	50.63	False
-840	-194	$103.9^{+0.8}_{-0.5}$	$7.88^{+0.13}_{-0.18}$	$5.50^{+2.40}_{-6.52}$	50.74	True
-600	-194	$80.3^{+2.4}_{-2.7}$	$6.12^{+0.53}_{-0.56}$	$16.30^{+1.07}_{-1.10}$	51.04	True
-600	194	$80.3^{+2.4}_{-2.7}$	$6.12^{+0.53}_{-0.56}$	$-16.30^{+1.10}_{-1.07}$	51.04	True
-488	-388	$85.2^{+0.7}_{-1.5}$	$5.70^{+0.87}_{-0.22}$	$38.00^{+7.10}_{-2.47}$	51.22	True
-360	194	$45.8^{+1.5}_{-0.2}$	$3.85^{+0.58}_{-1.02}$	$-26.50^{+1.71}_{-6.77}$	51.18	False
-240	-388	$24.0^{+10.7}_{-11.7}$	$4.00^{+0.61}_{-0.59}$	$58.50^{+8.41}_{-9.34}$	51.35	False
-120	194	$-11.0^{+6.6}_{-6.4}$	$2.00^{+0.32}_{-0.32}$	$-55.00^{+9.97}_{-8.20}$	51.48	False
0	0	$0.0^{+18.8}_{-8.5}$	$0.00^{+0.75}_{-0.45}$	$0.00^{+0.00}_{-0.00}$	51.64	False
120	-194	$-10.0^{+14.2}_{-12.6}$	$1.60^{+0.67}_{-0.61}$	$100.00^{+41.17}_{-12.11}$	51.47	False
240	-388	$35.0^{+2.5}_{-2.0}$	$3.30^{+0.18}_{-0.07}$	$117.00^{+1.12}_{-3.37}$	51.45	False
240	0	$0.0^{+19.4}_{-7.1}$	$1.50^{+0.57}_{-0.52}$	$180.00^{+20.96}_{-20.96}$	51.60	False
360	194	$0.0^{+9.2}_{-8.7}$	$2.70^{+0.33}_{-0.52}$	$-151.00^{+10.12}_{-8.83}$	51.39	False
480	-388	$49.0^{+4.7}_{-5.5}$	$4.18^{+0.27}_{-0.22}$	$134.70^{+3.61}_{-3.49}$	51.32	False
-380	0	$46.6^{+1.9}_{-4.4}$	$3.70^{+0.99}_{-0.46}$	$0.00^{+10.16}_{-10.16}$	51.26	True
380	0	$0.0^{+10.3}_{-10.2}$	$2.40^{+0.49}_{-0.45}$	$180.00^{+0.00}_{-0.00}$	51.53	False
-285	495	$7.4^{+0.6}_{-4.4}$	$4.75^{+0.70}_{-0.71}$	$-55.70^{+8.89}_{-8.95}$	51.40	True
-95	495	$8.2^{+9.8}_{-0.7}$	$4.00^{+0.22}_{-0.24}$	$-72.97^{+3.36}_{-3.45}$	51.44	True
95	-495	$14.0^{+14.4}_{-13.6}$	$3.80^{+0.70}_{-0.72}$	$93.00^{+11.27}_{-11.08}$	51.38	False
285	495	$52.0^{+0.3}_{-1.9}$	$4.10^{+0.34}_{-0.26}$	$-114.00^{+13.38}_{-1.33}$	51.20	True
190	-660	$62.0^{+6.0}_{-6.3}$	$5.20^{+0.37}_{-0.29}$	$104.00^{+3.45}_{-4.22}$	51.21	False
-388	660	$75.0^{+0.7}_{-2.4}$	$6.60^{+0.84}_{-0.16}$	$-57.35^{+0.86}_{-11.49}$	51.02	False
-800	-300	$105.0^{+9.5}_{-3.2}$	$8.70^{+0.11}_{-0.41}$	$25.30^{+2.48}_{-2.76}$	50.92	False
-880	-250	$111.2^{+2.5}_{-1.4}$	$8.60^{+0.22}_{-0.89}$	$19.00^{+3.43}_{-2.57}$	50.77	True
-560	-100	$71.9^{+1.5}_{-0.1}$	$5.30^{+1.17}_{-0.54}$	$11.10^{+0.75}_{-6.22}$	51.19	True
-680	-190	$96.4^{+10.9}_{-35.0}$	$6.60^{+0.96}_{-0.49}$	$13.80^{+2.26}_{-0.44}$	51.02	True
-530	-190	$77.9^{+11.3}_{-11.3}$	$5.30^{+1.07}_{-0.42}$	$17.80^{+2.76}_{-1.01}$	51.13	True
-630	-280	$88.8^{+3.3}_{-0.3}$	$6.40^{+0.49}_{-0.09}$	$20.70^{+2.21}_{-0.17}$	50.89	True
-850	-100	$102.0^{+5.7}_{-3.5}$	$8.20^{+0.16}_{-0.61}$	$12.20^{+0.57}_{-0.32}$	50.95	False
-270	-360	$35.0^{+0.4}_{-4.1}$	$3.50^{+1.04}_{-0.06}$	$40.10^{+17.14}_{-0.82}$	51.46	False
-370	-270	$56.0^{+1.3}_{-3.6}$	$4.30^{+0.54}_{-0.32}$	$30.70^{+12.04}_{-2.55}$	51.43	True
-800	-50	$96.5^{+7.2}_{-7.9}$	$7.50^{+0.48}_{-0.53}$	$12.80^{+0.83}_{-1.01}$	51.01	True
-700	-50	$86.6^{+0.2}_{-0.4}$	$6.70^{+0.49}_{-0.58}$	$13.90^{+1.06}_{-1.14}$	51.13	False
-500	-50	$63.0^{+10.3}_{-10.1}$	$4.90^{+0.62}_{-0.55}$	$17.90^{+1.81}_{-1.46}$	51.30	True
-600	-50	$75.5^{+3.2}_{-3.0}$	$5.80^{+0.21}_{-0.17}$	$15.10^{+0.18}_{-3.09}$	51.23	True
-200	100	$22.0^{+13.3}_{-12.9}$	$2.10^{+0.68}_{-0.62}$	$-25.00^{+17.56}_{-17.54}$	51.54	False
200	100	$23.0^{+13.8}_{-14.0}$	$1.70^{+0.61}_{-0.68}$	$-151.00^{+22.29}_{-22.50}$	51.48	False
-100	250	$30.0^{+12.8}_{-12.8}$	$2.50^{+0.61}_{-0.66}$	$-65.00^{+14.22}_{-15.19}$	51.48	False
-600	400	$90.6^{+6.6}_{-6.6}$	$6.50^{+0.62}_{-0.29}$	$-21.00^{+0.36}_{-0.80}$	50.97	True
-700	250	$94.0^{+5.1}_{-6.0}$	$7.10^{+0.40}_{-0.33}$	$-23.00^{+2.84}_{-2.98}$	51.08	False
-500	250	$74.0^{+9.3}_{-10.1}$	$5.60^{+0.54}_{-0.61}$	$-29.00^{+6.30}_{-5.61}$	51.25	False
-750	0	$91.3^{+6.4}_{-6.4}$	$7.00^{+0.58}_{-0.30}$	$0.00^{+3.37}_{-3.37}$	51.10	True
-800	-600	$80.0^{+9.9}_{-9.6}$	$8.70^{+0.68}_{-0.63}$	$31.00^{+4.46}_{-4.76}$	50.81	False
-600	-600	$61.0^{+3.5}_{-4.0}$	$8.00^{+0.06}_{-1.15}$	$30.00^{+1.85}_{-0.22}$	51.06	False
-450	100	$59.0^{+6.3}_{-6.8}$	$4.70^{+0.34}_{-0.40}$	$-13.00^{+4.54}_{-4.53}$	51.35	False
-650	-350	$93.5^{+3.6}_{-3.6}$	$7.00^{+0.20}_{-0.28}$	$20.00^{+1.33}_{-0.14}$	51.01	True
-650	-100	$82.8^{+9.9}_{-9.8}$	$6.39^{+0.62}_{-0.62}$	$10.00^{+5.47}_{-5.63}$	51.19	False
-580	0	$72.1^{+4.1}_{-1.5}$	$5.00^{+0.38}_{-0.12}$	$0.00^{+4.49}_{-4.49}$	51.12	True
-850	0	$96.6^{+0.5}_{-0.6}$	$7.00^{+0.13}_{-0.17}$	$0.00^{+4.34}_{-4.34}$	50.95	True
-750	-100	$93.0^{+3.9}_{-3.9}$	$7.21^{+0.27}_{-0.26}$	$9.10^{+1.97}_{-2.15}$	51.09	False
-350	-350	$26.3^{+0.2}_{-2.0}$	$5.00^{+0.31}_{-0.04}$	$47.00^{+7.50}_{-11.30}$	51.17	False

Notes.
[a]Error values were obtained only for variable parameters and within 0.01 dB
[b]*True* or *False* column indicates whether the result was a primary or a secondary peak of the response function of the telescope for those locations of x and y.

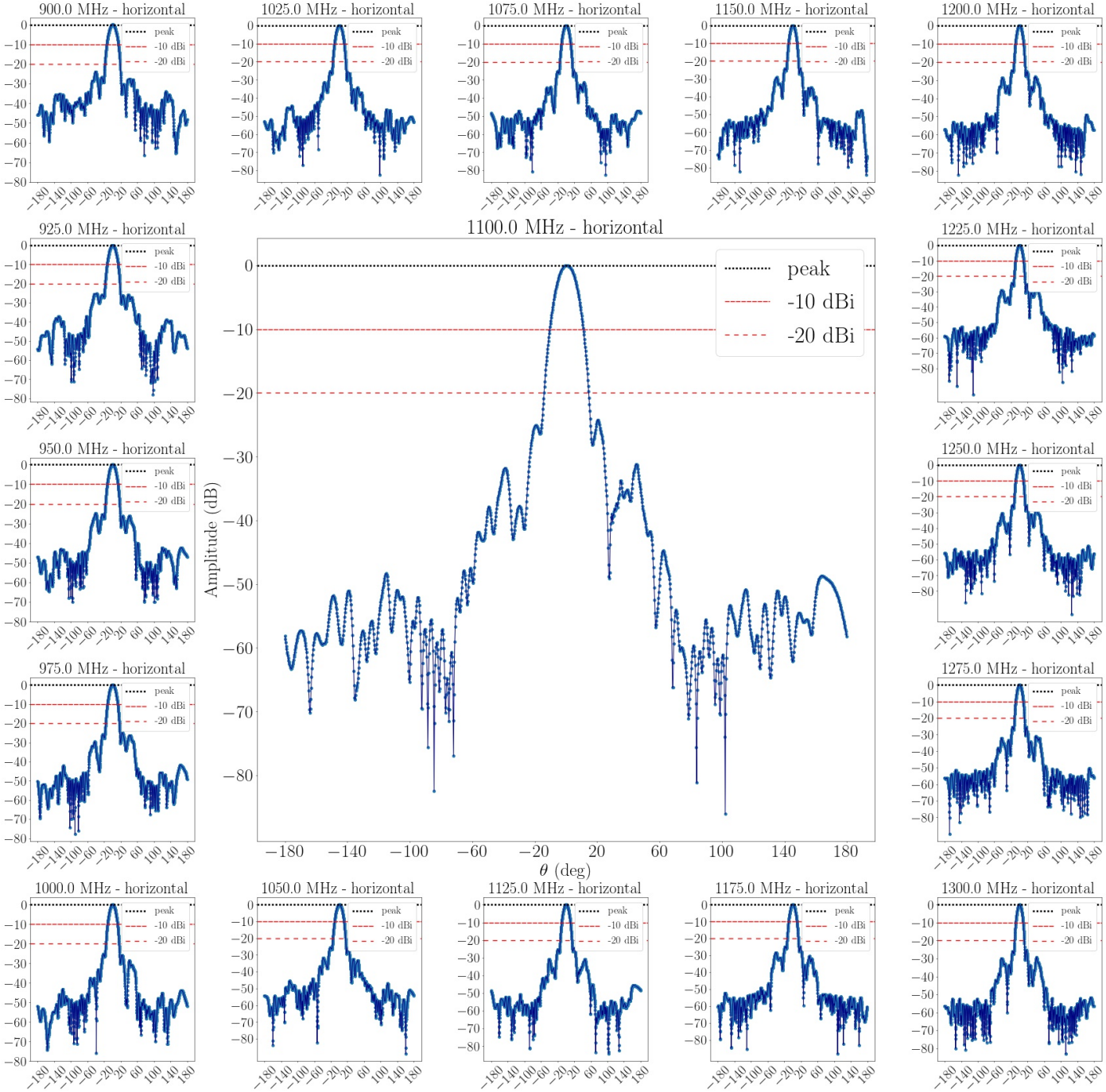

Fig. C.1: Plots from the horn beam measurements from Wuensche et al. (2020) used to obtain the 10-20 dB attenuation angles as a function of frequency for a horizontally polarized input signal. For each plot the intensity is attenuated by 10 dB (red dashed line) and 20 dB (sparse red dashed line) in relation to the peak intensity (black dashed line).

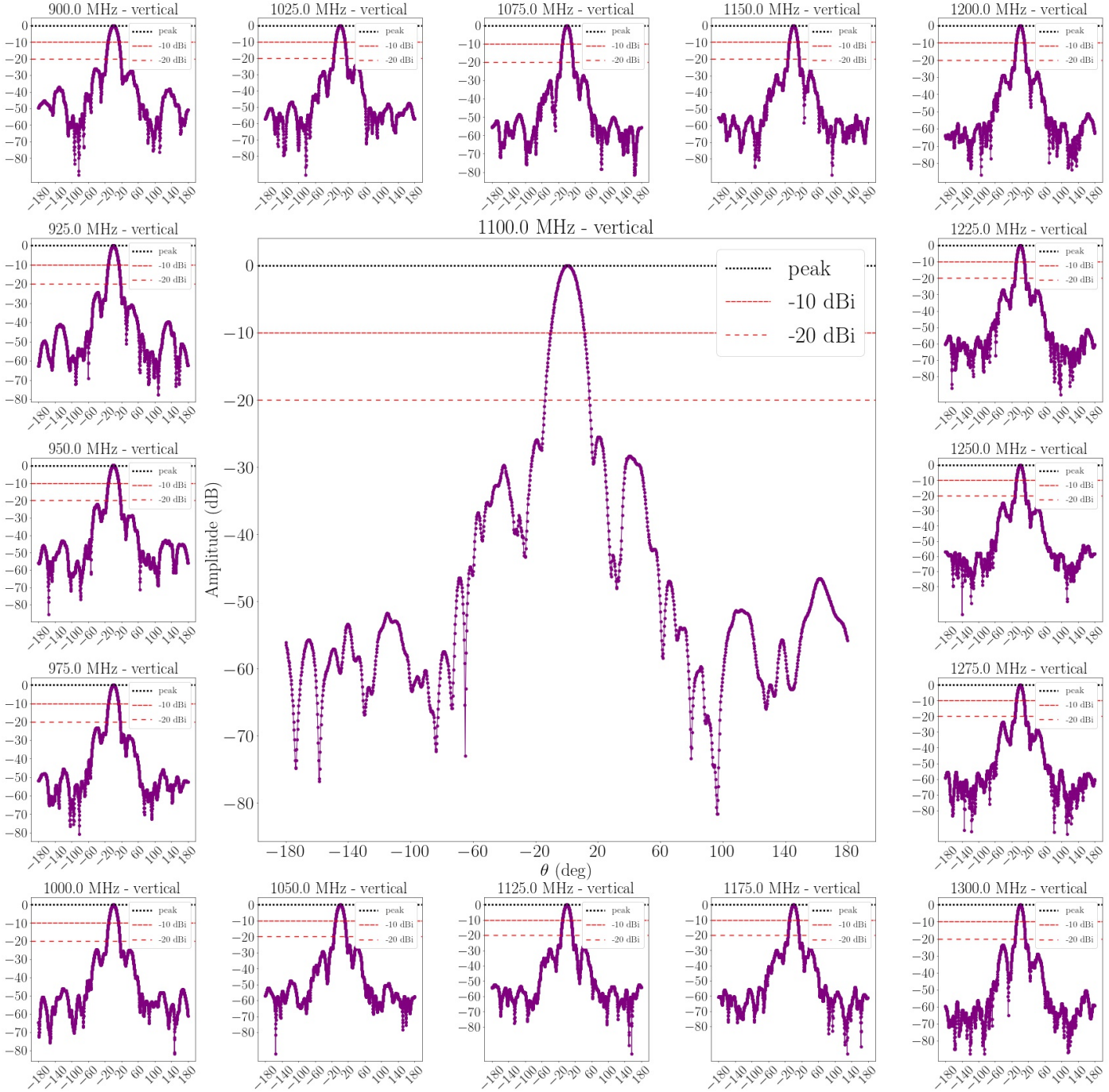

Fig. C.2: Plots from the horn beam measurements from Wuensche et al. (2020) used to obtain the 10-20 dB attenuation angles as a function of frequency for a vertically polarized input signal. For each plot the intensity is attenuated by 10 dB (red dashed line) and 20 dB (sparse red dashed line) in relation to the peak intensity (black dashed line).